ACS OMEGA

http://pubs.acs.org/journal/acsodf

Article

Design and Computational Analysis of an MMP9 Inhibitor in Hypoxia-Induced Glioblastoma Multiforme

Smita Kumari and Pravir Kumar*

Cite This: *ACS Omega* 2023, 8, 10565−10590

Read Online

ACCESS | Metrics & More | Article Recommendations | Supporting Information

ABSTRACT: The main therapeutic difficulties in treating hypoxia-induced glioblastoma multiforme (GBM) are toxicity of current treatments and the resistance brought on by the microenvironment. More effective therapeutic alternatives are urgently needed to reduce tumor lethality. Hence, we screened plant-based natural product panels intending to identify novel drugs without elevating drug resistance. We explored GEO for the hypoxia GBM model and compared hypoxic genes to non-neoplastic brain cells. A total of 2429 differentially expressed genes expressed exclusively in hypoxia were identified. The functional enrichment analysis demonstrated genes associated with GBM, further PPI network was constructed, and biological pathways associated with them were explored. Seven webtools, including GEPIA2.0, TIMER2.0, TCGA-GBM, and GlioVis, were used to validate 32 hub genes discovered using Cytoscape tool in GBM patient samples. Four GBM-specific hypoxic hub genes, LYN, MMP9, PSMB9, and TIMP1, were connected to the tumor microenvironment using TIMER analysis. 11 promising hits demonstrated positive drug-likeness with nontoxic characteristics and successfully crossed blood−brain barrier and ADMET analyses. Top-ranking hits have stable intermolecular interactions with the MMP9 protein according to molecular docking, MD simulation, MM-PBSA, PCA, and DCCM analyses. Herein, we have reported flavonoids, 7,4′-dihydroxyflavan, (3*R*)-3-(4-hydroxybenzyl)-6-hydroxy-8-methoxy-3,4-dihydro-2*H*-1-benzopyran, and 4′-hydroxy-7-methoxyflavan, to inhibit MMP9, a novel hypoxia gene signature that could serve as a promising predictor in various clinical applications, including GBM diagnosis, prognosis, and targeted therapy.

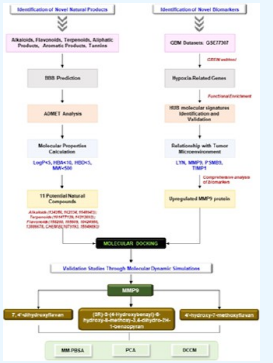

1. INTRODUCTION

According to CBTRUS (Central Brain Tumor Registry of the United States), 2021 recent research, glioblastoma multiforme (GBM) accounts for 48.6% of primary malignant brain tumors. Individuals aged 20−39 years experienced the most significant increases in survival, with 5 year survival increasing from 44 to 73%. In contrast, the failure to enhance survival in older age groups was primarily due to the inability to improve GBM therapy.[1] Currently, GBM is being treated with a combination of surgery, radiation therapy, and chemotherapeutics [alkylating drug temozolomide (TMZ) and antiangiogenic agent bevacizumab]. Furthermore, novel treatments such as tumor-treating fields and immunotherapy offer promise for a better prognosis.[2] Despite these treatment options, GBM patients' overall survival and quality of life remain dismal. The plethora of research mentioned numerous obstacles to GBM treatment, including tumor heterogeneity, acidic microenvironment, and immunosuppression, all of which are linked to the hypoxic environment to some degree.[3]

GBM, being a highly vascularized human tumor, its microcirculation is poor, resulting in the hypoxia region inside the tumor. In the tumor microenvironment (TME), unregulated cell proliferation in the tumor (tumor size exceeds the diameter of >1 mm) often surpasses the capacity of the pre-existing blood capillaries to meet the oxygen demand.[4] This results in a condition known as hypoxia, which impairs the availability of nutrients and promotes genetic instability because of an increase in the generation of reactive oxygen species making it a crucial factor for tumorigenesis. As the master regulator orchestrating cellular responses to hypoxia, hypoxia-inducible factor 1 (HIF-1) plays an essential role in GBM aggressiveness. This modulates the expression of angiogenic factors, such as vascular endothelial growth factor (VEGF), insulin-like growth factor II, and platelet-derived growth factor B (PDGF), and several glucose and fatty acid metabolism factors, the tumor-immune microenvironment, and stimulation of the epithelial−mesenchymal transition (EMT), suppressing apoptosis and promoting autophagy.[5,6] In addition, hypoxia also serves as a niche environment for the aggregation of cancer stem cells, which promotes carcinogenesis and resistance. Tumor cells use a variety of strategies in response to hypoxia, including the expulsion of cytotoxic anticancer drug by ABC-transporters, manifesting a dormant state and exhibiting pluripotency (stemness) traits, which can lead to the failure of existing therapy.[7] Studies showed that hypoxia promotes secretion of cytokines and chemokines which affects immunosurveillance by affecting CD8+ T cell infiltration and disrupting

Received: January 21, 2023
Accepted: February 28, 2023
Published: March 13, 2023

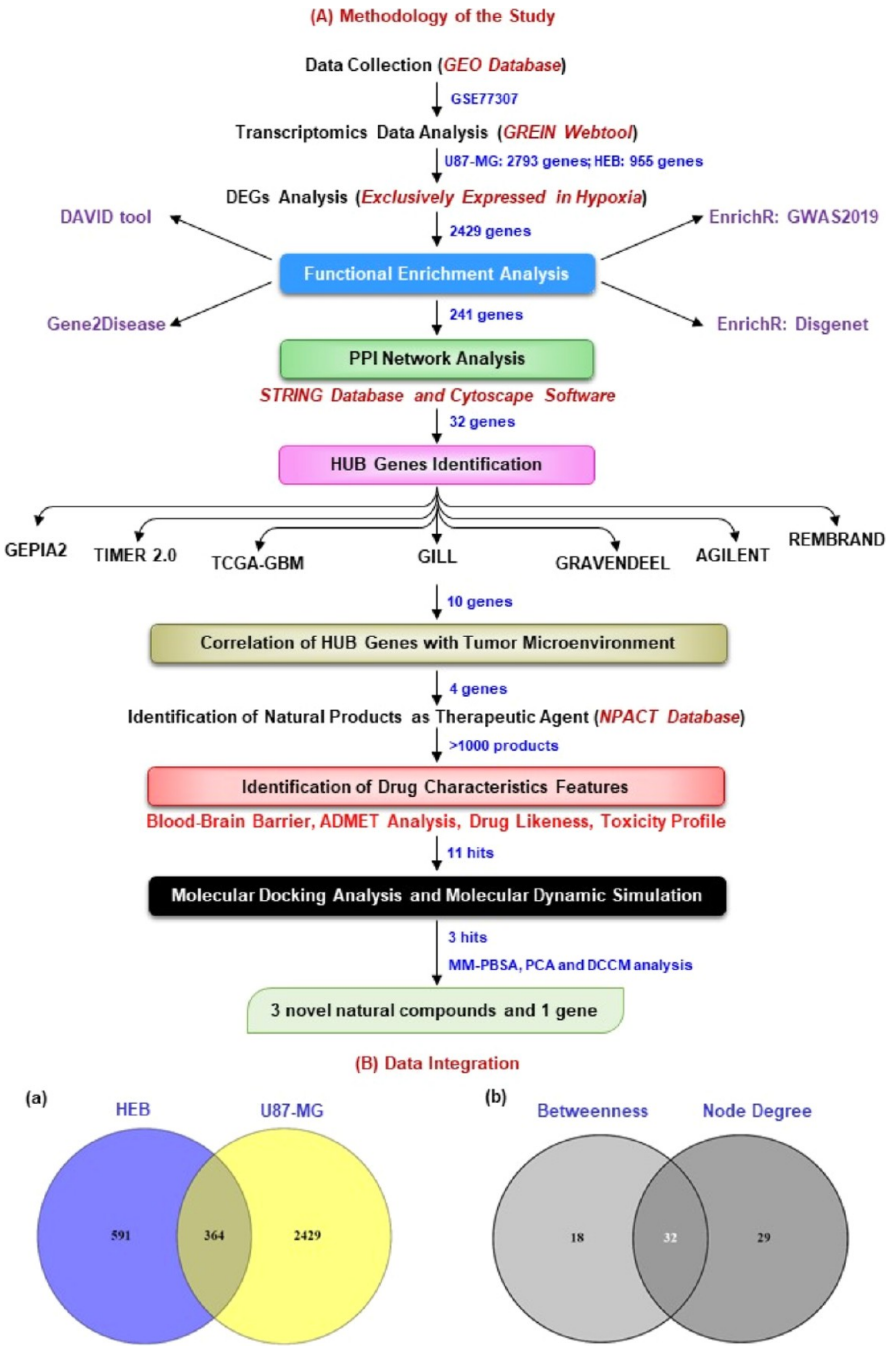

Figure 1. (A) Workflow scheme for identification of novel natural compounds (target) against GBM-hypoxia microenvironment. (B) Interactive Venn analysis: (a) identification of DEGs in the GBM-hypoxia microenvironment. A total of 2429 altered DEGs exclusively expressed in hypoxia were identified from the GSE77307 data set using the GREIN tool. The "cross areas" are common DEGs in both cell lines. The cutoff criteria were p value $\leq$ 0.05 and [log fold change] $\geq \pm 1.5$. (b) A total of 32 hub genes among topology parameters (betweenness and degree) were identified from Cytoscape software. The "cross areas" are common hub genes. HEB (purple): non-neoplastic brain cell; U87-MG (yellow): human GBM cell model.

the cytotoxicity of natural killer cells cells. In addition, hypoxic tumor-associated macrophages reduce T cell responses and encourage tumor proliferation and angiogenesis.[8,9] Another essential piece of research emphasizes the role of $\gamma\delta$ T cells as they do not require antigen presentation for activation compared to conventional T cells and are thus an excellent therapeutic target for brain tumors. This pathway is also mediated by hypoxia.[10] So, given hypoxia's critical role in intratumoral interactions, identifying targets that induce adaptation to the hypoxic niche is crucial for a better understanding of GBM origin, development, and treatment resistance.[11] Indeed, "hypoxia" is an essential driving force of GBM and could be used as a novel treatment tool.[12]

Regardless of the fact that there have been few improvements in the progression of GBM therapies to boost patient survival, researchers and clinicians are indeed eager to study novel therapies and techniques for treating this disease.[13] Natural compounds and their structure analogues have been the source of most medicines' active ingredients for various indications, including cancer.[14] Some widely used plant-derived natural compounds are etoposide, irinotecan, paclitaxel, and vincristine, bacteria-derived anti-cancer therapeutics are mitomycin C and

https://doi.org/10.1021/acsomega.3c00441
ACS Omega 2023, 8, 10565−10590

actinomycin D, and marine-derived anti-cancer therapeutics is bleomycin.[15] Numerous studies suggest that natural compounds are used as chemosensitizers (such as quercetin, resveratrol, withaferin A, etc.), radiosensitizers (such as tetrandrine, zataria, multiflora, and guduchi), and anti-proliferative (such as curcumin, oridonin, rutin, and cucurbitacin) alkaloids and flavonoid agents.[16,17] Identification of new drugs that can modify the BBB (blood−brain barrier), decrease the tumor growth, and prevent the development of recurring tumors is critical for improving overall patient prognosis. In vitro and/or in vivo, various natural compounds with well-established biological benefits have oncologic effects on GBM.[18] These include flavonoids, terpenoids, alkaloids, tannins, coumarins, curcuminoids, terpenes, lignans, natural steroids, and plant extracts.[19] Statistics show that over 60% of the approved anti-cancer agents are of natural origin (natural compounds or synthetic compounds based on natural product models).

The present study conducted transcriptomic analysis between hypoxia and normoxia (in both normal non-neoplastic brain cells and GBM tumor cells) samples to screen differentially expressed genes (DEGs) related to hypoxia effects. Comprehensive bioinformatics and computational methodologies were used to identify hub genes (LYN, MMP9, PSMB9, and TIMP1) and significant modules and pathways related to the TME. We found that matrix metalloproteinase 9 (MMP9) plays a vital role as a hypoxic gene signature, which has the potential to be used as a biomarker. Numerous studies have also shown the dysregulation of MMP9 in the microenvironment associated with hypoxia and cancer.[20] MMP9 can cleave and remodel extracellular matrix (ECM) proteins such as collagens and elastin involved in invasion, metastasis, and angiogenesis.[21] MMP9 is produced de novo by monocytes and inflammatory macrophages, as well as most cancer cells, during stimulation induced by various extracellular signals present in TME, such as proinflammatory cytokines (such as TNF-α, IL-8, and IL-1β) and growth factors (such as TGF-β, PDGF, and bFGF), which can bind to their receptors and activate downstream signaling cascades involved in the activation of transcription factors including NF-κB, SP1, AP1, and HIF-1α. This affects various downstream biological processes, including matrix degradation, remodeling, EMT, enhanced tumoral invasion, metastasis, angiogenesis, inflammation, drug resistance, and so forth; hence, it acts as a challenging target for targeted therapy for cancer.[22]

Targeting TME has been a significant focus in recent years, and hence MMP inhibitors that will target a hypoxia condition in the microenvironment could be of great significance as a new antitumor agent. For this purpose, we have availed network pharmacology, structure-based drug design approach such as molecular docking, molecular dynamics (MD) simulation analysis, and molecular mechanics Poisson−Boltzmann surface area (MM-PBSA) approach to discover prospective classes of natural compounds with druggable and nontoxic properties from the plant-based natural compounds library. We identified 11 hits based on the particular interaction that satisfy the ADMET and LIPINSKI rule of five analyses, pass the toxicity profile, and have a significant affinity for the MMP9 binding site domain. The three best-docked compounds were further subjected to MDS for 50 ns to understand protein−ligand complex stability. Previously also, researchers have explored the potential of alkaloids and flavonoids for anti-cancer treatments.[23,24] Drugs, including natural compounds that target MMP9, have not been used in the clinical setting. Therefore, targeted MMP9 drugs must be screened for treating patients with GBM. Our results can potentially benefit from managing GBM malignancy caused by a hypoxia microenvironment. The findings of this study contribute to a better understanding of the role of the hypoxia microenvironment. Figure 1A depicts the process of the methodologies used in this investigation.

2. MATERIALS AND METHODS

2.1. Data set Acquisition and Processing. The NCBI-Gene Expression Omnibus (NCBI-GEO; https://www.ncbi.nlm.nih.gov/geo) database[25] is a publicly accessible library of next-generation sequencing, RNA sequencing, and microarray profiling used to gather GBM and non-neoplastic brain tissue gene expression profiles from GEO accession number, GSE77307. The transcriptome data in GSE77307 were derived from GPL11154, a platform using Illumina HiSeq 2000 (*Homo sapiens*). This included three replicates of each U87-MG cell line as a human GBM cancer cell model and the human brain HEB cell line as a non-neoplastic brain cell model cultured in 21% oxygen (normoxia) and 1% oxygen (hypoxia) for transcriptional profiling. This data set was chosen due to the availability of only one data set in the database based on the filter (glioblastoma; hypoxiaTME). High-throughput functional transcriptomic expression data from GSE data sets were analyzed through GEO RNA-seq Experiments Interactive Navigator online server (GREIN; https://shiny.ilincs.org/grein).[26] GREIN is provided by the backend compute pipeline for uniform processing of RNA-seq data and large numbers (>65,000) of processed data sets.

2.2. Enrichment Analysis of Identified DEGs. Transcriptomics data analysis was performed using the GREIN web tool. DEGs were determined by comparing their expression levels in hypoxia (1% oxygen) versus normoxia (21% oxygen) in GBM cells, U87-MG, and normal brain cells, HEB. Statistically significant DEGs were screened using cutoff filter criteria such as unpaired t-test and p-value ≤ 0.05, false discovery rate ≤ 0.05, and [log fold change] ≥ 1.5. DEGs only exclusively expressed in hypoxia conditions were considered for further analysis. In addition, enrichment analysis of DEGs, including both upregulated and downregulated genes associated with GBM, was performed by utilizing different omics approaches such as the Database for Annotation, Visualization and Integrated Discovery (DAVID) functional annotation tool (https://david.ncifcrf.gov/),[27] gene set to diseases (GS2D) tool (http://cbdm.uni-mainz.de/geneset2diseases),[28] and Enrichr-GWAS2019 and Enrichr-DisGeNET of Enrichr tool (https://amp.pharm.mssm.edu/Enrichr)[29,30] to identify and prioritize the most significant genes associated with GBM. Furthermore, the biological pathway and functional enrichment analyses of candidate DEGs and hub genes were determined through a freely available software known as the FunRichr tool (version 3.1.3) (http://www.funrich.org/)[31] to identify the biological pathways associated with them.

2.3. Integration of Protein−Protein Interaction Network and Hub Genes Identification. The selected enriched genes were then examined for designing Protein−Protein Interaction (PPI) using an online Search Tool for the Retrieval of Interacting Genes/Proteins (version 11.5) (STRING, https://string-db.org/) for *H. sapiens*[32] that covers known and predicted interactions for different organisms. The experimentally significant interactions (with high confidence scores $\geq$ 0.700) were chosen to build a network model, while the others were excluded from the analysis. Cytoscape software (version

https://doi.org/10.1021/acsomega.3c00441
ACS Omega 2023, 8, 10565−10590

3.8.1) (https://cytoscape.org/)[33] was implemented to analyze the PPI network and identify the hub protein. To calculate the topological parameters such as the node degree (the number of connections to the hub in the PPI network) and betweenness (which corresponds to the centrality index of a particular node), we used the CentiScaPe plugin (version 2.2). It denotes the shortest route between two nodes. Genes with higher values than the average score were chosen.

2.4. Hub Protein Shorting and Validation. To verify and validate the expression of the shortlisted hub proteins, we have utilized both transcriptomics and genomics data from GBM patients. Different databases were explored for RNA sequencing data, such as GEPIA2.0, TIMER2.0, TCGA-GBM, and GlioVis-GILL, and microarray data, such as GlioVis-REMBRANDT, GlioVis-AGILENT, and GlioVis-Gravendeel based on Cancer Genome Atlas (TCGA)-GBM.[34−36] GEPIA2.0 analyzed the RNA sequencing expression data of 9736 cancers and 8587 normal samples from the TCGA and GTEx projects using a standard processing pipeline. GlioVis is a user-friendly web tool that allows users to study brain tumor expression data sets through data visualization and analysis. For GlioVis-GILL, Gill et al. conducted RNA-seq and histological examination on radiographically labeled biopsies collected from different regions of GBM.[37] GlioVis-Repository of Molecular Brain Neoplasia Data (REMBRANDT), a cancer clinical genomics database and a web-based data mining and analysis platform, includes data produced from 874 glioma specimens with approximately 566 gene expression arrays and 834 copy number arrays generated through the Glioma Molecular Diagnostic Initiative.[38] In GlioVis-Gravendeel, gene expression profiling was carried out on a large cohort of glioma samples from all histologic subtypes and grades.[39] In TIMER2.0, multiple immune deconvolution algorithms were used to assess the quantity of immunological infiltrates. Its Gene DE module allows users to investigate the differential expression of any gene of interest in tumors and surrounding normal tissues across all TCGA tumors. All hub genes significantly expressed in all seven patient GBM databases were chosen for subsequent research. Finally, shortlisted genes were again subjected to Tumor IMmune Estimation Resource (TIMER) (https://cistrome.shinyapps.io/timer)[40] analysis. Here, we utilized this database to link hub gene expression with tumor purity and estimate the infiltration levels of six immune cell types [CD4+ T cells, CD8+ T cells, B cells, macrophages, neutrophils, and dendritic cells (DCs)] in GBM data sets. This tool calculates immune infiltration based on immune subsets' preset characteristic gene matrix.

2.5. Localization Study and Construction of Transcription Factor-Gene Network. CELLO (http://cello.life.nctu.edu.tw/cello.html): subcellular localization predictor combines a two-level support vector machine system and the homology search method-based tool to predict the subcellular localization of the protein.[41] Regulatory transcription factors (TFs) that control the expression of genes at the transcriptional level were obtained using the JASPAR database, containing curated and nonredundant experimentally defined TF binding sites.[42] The TF-gene interaction networks were constructed and analyzed with NetworkAnalyst (version3.0) (https://www.networkanalyst.ca/).[43]

2.6. Identification of Natural Compounds and Blood−Brain Permeability Prediction. The plant-derived natural compounds with known anti-cancer bioactivity information were obtained from a literature survey through PubMed and the central resource Naturally Occurring Plant-based Anti-cancer Compound-Activity-Target database (NPACT, http://crdd.osdd.net/raghava/npact/).[44] This database, which presently has 1574 compound entries, collects information on experimentally confirmed plant-derived natural compounds with anticancer action (in vitro and in vivo). We have chosen terpenoids (513 entries), flavonoids (329 entries), alkaloids (110 entries), polycyclic aromatic natural compounds (63 entries), aliphatic natural compounds (20 entries), and tannin (6 entries).BBB obstructions make it difficult to create drugs to treat brain cancer. The BBB blocks the uptake of necessary therapeutic drugs into the brain. The epithelial-like tight connections seen in the brain capillary endothelium are the source of this characteristic. For the treatment of GBM, it is crucial to screen drugs that have the ability to cross the BBB.[45] While designing a drug for brain diseases, physicochemical properties and brain permeation properties should be optimized. In consideration of this challenge, we analyzed our candidate natural compounds for physicochemical properties using the SwissADME (http://www.swissadme.ch/)[46] analysis tool and the CBLigand (version 0.90) online BBB predictor (https://www.cbligand.org/BBB/).[47]

2.7. Prediction of Molecular Properties and Drug Toxicity. Each natural compound's molecular formula (MF), molecular weight (MW), hydrogen bond acceptor (HBA), hydrogen bond donor (HBD), log *P* value, and SMILES were retrieved using the PubChem chemical database (https://pubchem.ncbi.nlm.nih.gov/). The Lipinski rule of five was used to estimate the druggability of each phytocompound using the SMILES data of individual compounds on the MolSoft web server (https://molsoft.com/mprop/).[48] The server includes structural data such as MF, MW, HBA, HBD, and logP and a drug-likeness score prediction (DLS). The toxicity and pharmacokinetics of natural compounds with positive DLS were also predicted using the ADMETlab 2.0 (https://admetmesh.scbdd.com/) webserver.[49]

2.8. Molecular Docking Studies. *2.8.1. Preparation of Ligand.* Based on the network analysis and pharmacology approach, 11 natural compounds, viz., 6 flavonoids, 3 alkaloids, and 2 terpenoids, were qualified for all criteria required for being used as a drug candidate. Thus, the three-dimensional (3D) structures of 11 natural compounds along with 2 reference drugs (one natural compound and one conventional standard molecule) were retrieved from the PubChem database (https://pubchem.ncbi.nlm.nih.gov/) in the structure data file (.sdf) format. These structures additionally went through the dock prep section of Discovery Studio Visualizer[50] (BIOVIA Discovery Studio Visualizer; https://discover.3ds.com/discovery-studio-visualizer-download) 2019. The conjugate gradients algorithm was used to minimize the ligand structures using the "uff" forcefield.[51] The polar hydrogens and Gasteiger charges were added to the ligands to convert them into the ".pdbqt" format.

2.8.2. Preparation of Protein. Based on the network analysis and TIMER analysis, the overexpressed MMP9 gene associated with the TME was prioritized for future investigation. The Research Collaboratory for Structural Bioinformatics (RCSB; https://www.rcsb.org/) protein data bank was used to retrieve the X-ray crystallographic structure of MMP9 (PDB: 4HMA). Further, the PrankWeb (https://prankweb.cz/) server based on P2Rank, a machine learning method, was used to retrieve the information on the target active site and binding pockets, and the ligand was docked within the predicted site. Functional characteristics of protein structures were validated using

https://doi.org/10.1021/acsomega.3c00441
ACS Omega 2023, 8, 10565−10590

Ramachandran plot, ERRAT, and VERIFY3D.[52−54] For a good quality model, the ERRAT quality factor should be greater than 50, and the number of residues having a score ≥ 0.2 in the 3D/1D profile, as predicted by the VERIFY3D server, should be more than 80%.

2.8.3. Protein−Ligand Docking. All ligands were docked against protein using AutoDock vina 4.0 executed through the POAP pipeline.[55] The intermolecular interaction compounds showing the least binding energy and maximum intermolecular interaction with the active site residues were selected to visualize protein−ligand interactions using BIOVIA Discovery Studio Visualizer 2019 and further subjected for MD simulation.

2.9. MD Simulation of Best-Docked Protein−Ligand Complex. In order to infer the stability of docked complexes, we prioritized five complexes (three test and two standard complexes) and subjected to all-atoms explicit MD simulation for 50 ns production run using GROMACS version 2021.3 software package (GNU, General Public License; http://www.gromacs.org).[56] The ligand and protein topology were generated using Amber ff99SB-ildn force field (https://ambermd.org/AmberTools.php) via antechamber x-leap tool. The system was solvated using the TIP3P water model in an orthorhombic box with a boundary condition of 10.0 Å from the edges of the protein in all directions. The system was neutralized by adding necessary amounts of counterions. The conjugate gradient approach was employed to obtain the near-global state least-energy conformations after the steepest descent. Canonical (constant temperature, constant volume, *NVT*) and isobaric (constant temperature, constant pressure, *NPT*) equilibrations were performed on the systems for 1 ns. A modified Berendsen thermostat method was used in *NVT* equilibration to keep both the volume and temperature constant (300 K). Similarly, a Parrinello−Rahman barostat was used during *NPT* equilibration to keep the pressure at 1 bar constant. The particle mesh Ewald approximation was used with a 1 nm cutoff to calculate the long-range electrostatic interactions, van der Waals interactions, and coulomb interactions. In order to control the bond length, the LINCS algorithm (LINear Constraint Solver algorithm) was utilized. The coordinates were recorded every two fs during each complex's production run of 50 ns. In-built GROMACS utilities were used to evaluate the generated trajectories, and other software packages were incorporated where necessary for a more specialized analysis. MD trajectories were analyzed to determine the c-alpha root-mean-square fluctuation (RMSF) and root-mean-square deviation (RMSD) of the backbone and complex, the protein radius of gyration (R_g), the protein solvent-accessible surface area (SASA), and the number of hydrogen bonds between the protein and the ligand.

2.10. Investigation of Binding Affinity Using MM-PBSA. It is standard procedure to use the relative binding energy of a protein−ligand complex in MD simulations and thermodynamic calculations. MM-PBSA was performed by "g_mmpbsa" tool.[57] The total free energy of each of the three entities (ligand, protein receptor, and complex) mentioned can be calculated by adding the potential energy of the molecular mechanics and the energy of solvation. Early research work[58,59] was used to obtain the parameter that was used to determine the binding energy.

$$\Delta G_{(\text{binding})} = G_{(\text{complex})} - G_{(\text{protein})} - G_{(\text{ligand})} \quad (1)$$

where $G_{(\text{complex})}$ is the total free energy of the ligand−protein complex and $G_{(\text{protein})}$ and $G_{(\text{ligand})}$ are the total free energies of the isolated protein and ligand in the solvent, respectively.

The binding energy was calculated over the stable trajectory observed between 50 ns using 50 representative snapshots.

2.11. PCA and DCCM Analyses. Principal component analysis (PCA) was used in the current work to analyze the main types of molecular motions utilizing MD trajectories. It is employed to study the eigenvectors, which are crucial to understanding the overall movements of proteins during ligand binding. The "least square fit" to the reference structure is used to eliminate the molecule's translational and rotational mobilities. The "time-dependent movements" that the components carry out in a specific vibrational mode are demonstrated by projecting the trajectory onto a particular eigenvector. The average of the projection's time signifies the involvement of atomic vibration components in this form of synchronized motion. Using the "g_covar" and "g_anaeig" tools, which are already included in the GROMACS software package, the PCA was performed by first creating the covariance matrix of the Cα-atoms of the protein and then diagonalizing it. The *xmgrace* tool was used to plot the graphs.[60−62]

To determine if the motion between atom pairs is correlated (positive or negative), the dynamic cross-correlation matrix (DCCM) measures the magnitude of all pairwise cross-correlation coefficients. Herein, we investigated each element of DCCM, where C_{ij} = 1 representing the case of positively correlated fluctuations of atoms *i* and *j* have the same period and same phase, while C_{ij} = −1 and C_{ij} = 0, respectively, represent negatively or not correlated.[63,64]

2.12. Statistical Analysis. This study investigated the expression of hub genes in the GEPIA2.0 database and their connection with GBM using ANOVA. $|\log_2$ fold change$|$ cutoff ≤ 1.5 and *Q*-value ≤ 0.05 were considered significant. Tukey's Honest Significant Difference statistics were employed in the GlioVis database, where the *p*-value of the pairwise comparisons was used (***$p \le 0.001$; **$p \le 0.01$; *$p \le 0.05$; ns, not significant). In TIMER2.0, the Wilcoxon test's statistical significance was indicated by the number of stars (***$p \le 0.001$; **$p \le 0.01$; *$p \le 0.05$; ns, not significant). In the TIMER database analysis, a partial Spearman's correlation was applied. When $|\rho| > 0.1$, it indicated a correlation between the genes and immune cells. Significant data in the biological and KEGG pathway enrichment were screened according to *p*-value ≤ 0.05 with the Students' *t*-test.

3. RESULTS

3.1. Omics Data Mining and Identification of DEGs in GBM Hypoxia Condition. This study used the expression profile (GSE77307) from the NCBI-GEO database to identify DEGs exclusively expressed in hypoxia-induced GBM because targeting the hypoxic microenvironment could be a new tool for treatment.[7] Cells derived from GBM patient tumors and normal brain tissue were grown in hypoxic and normoxic conditions. GEO's raw RNA sequence (RNA-seq) data were processed and uploaded to GREIN using the GEO RNA-seq experiments processing (GREP2) pipeline. GREIN workflows with a graphical user interface provide complete interpretation, visualization, and analysis of processed data sets.[65] A normalized MA plot has been shown in Supporting Information Figure S1. GBM cancer cell model (U87-MG) and the human non-neoplastic brain cell model (HEB) were analyzed separately by comparing hypoxia with normoxia conditions to find dysregulated genes in hypoxia conditions. Subsequently, Venn's analysis demonstrated the involvement of 364 genes that were common in hypoxia conditions in both cell lines. 591 and 2429 genes

https://doi.org/10.1021/acsomega.3c00441
ACS Omega 2023, 8, 10565−10590

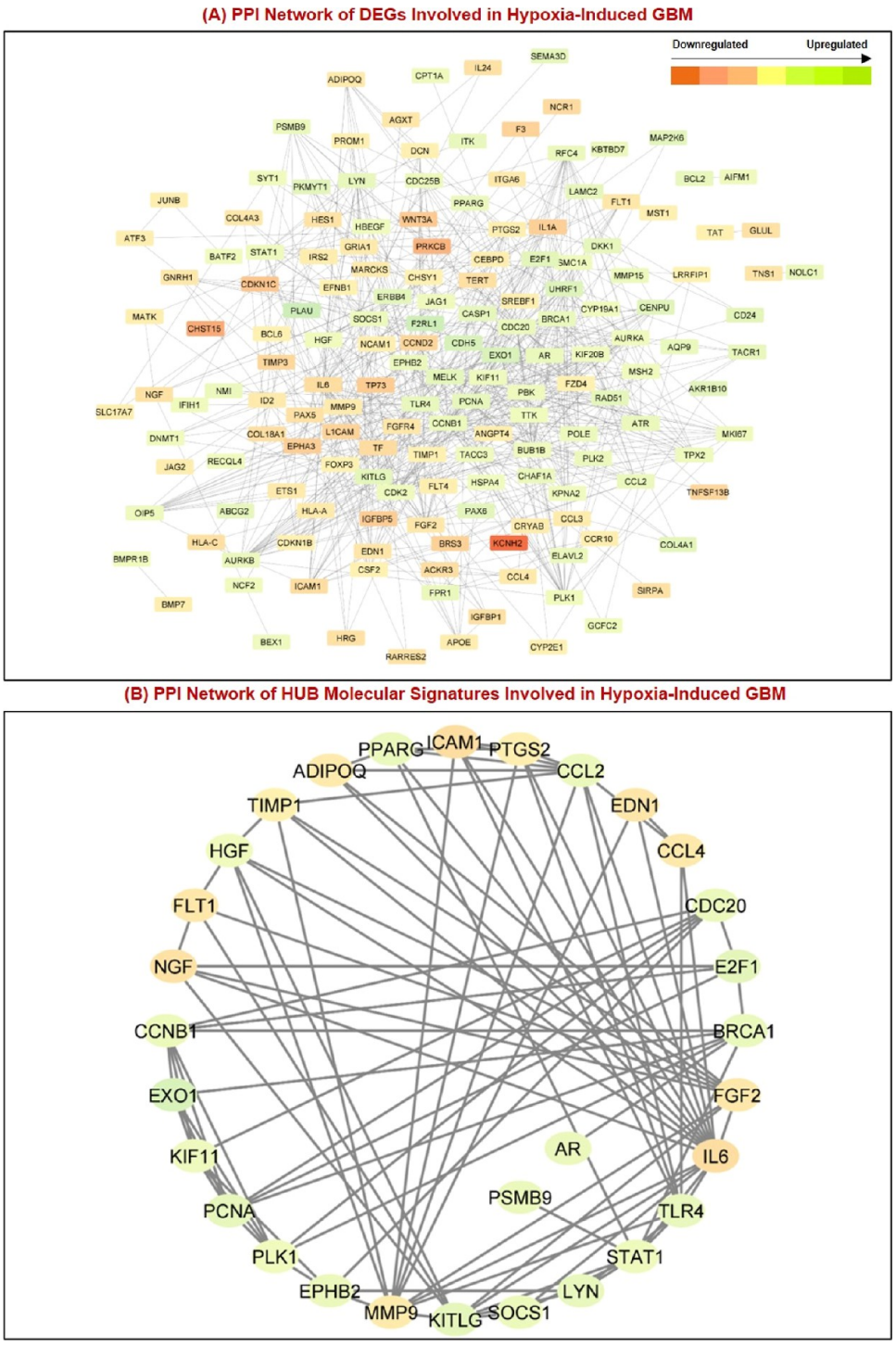

Figure 2. PPI network complex and modular analysis. (A) Module 1: a total of 241 DEGs (129 upregulated genes and 112 downregulated genes) were filtered into the DEG PPI network complex using STRING and Cytoscape software. It was composed of 163 nodes and 592 edges. (B) Module 2 showed a PPI network of 32 hub genes. Nodes in green signify upregulation and nodes in red signify downregulation. The colors from red to green represent the intensities of expression ($\log_2$ fold change, value: −6 to +14; cutoff value ±1.5), where red represents downregulation and green represents upregulation. In the presented figure, varying shades of red (from dark to light) show a decrease in the expression of downregulated genes, while shades of green (from light to dark) show increase in the expression of upregulated genes. Upregulated genes with $\log_2$ fold change ≥ 1.5 and downregulated genes with $\log_2$ fold change ≤ 1.5. STRING: Search Tool for the Retrieval of Interacting Genes/Proteins database.

expressed exclusively in hypoxia conditions in HEB and U87-MG cell lines, respectively.[66] Among them, we were interested in 2429 hypoxia-related DEGs exclusively expressed in hypoxia conditions and hence were considered for further analysis (Figure 1B,a). DAVID enrichment analysis of 2429 genes revealed that 30 genes have a significant association with GBM. In addition, G2SD enrichment (default cutoff parameter) showed 25 genes related to GBM. Similarly, GWAS-2019 and DisGeNET of Enrichr webtool enrichment analysis showed 3 and 242 genes linked with GBM, respectively. When we

https://doi.org/10.1021/acsomega.3c00441
ACS Omega 2023, 8, 10565−10590

Table 1. In Silico Expression Analysis and Validation of all 32 HUB Signatures Using Various Databases Containing Data from GBM Patient Samples[a]

Gene Name	RNA sequence dataset		Microarray datasets				
	GEPIA2	TIMER2.0	GlioVis				
			TCGA_GBM	GILL	REMBRANDT	AGILENT-4502a	Gravendeel
ADIPOQ							
AR							
BRCA1							
CCL2							
CCL4							
CCNB1							
CDC20							
E2F1							
EDN1							
EPHB2							
EXO1							
FGF2							
FLT1							
HGF							
ICAM1							
IL6							
KIF11							
KITLG							
LYN							
MMP9							
NGF							
PCNA							
PLK1							
PPARG							
PSMB9							
PTGS2							
SOCS1							
STAT1							
TF							
TIMP1							
TLR4							
SAMPLE SIZE							
GBM TUMOR	163	156	75	153	219	489	159
NORMAL TISSUES	207	4	17	5	28	10	8

[a]Dark green color = ***$p \leq 0.001$; medium green color = **$p \leq 0.01$; light green color = *$p \leq 0.05$; gray color = ns, not significant. In all seven GBM patient databases, including four RNA sequence data sets and three microarray data sets; the gene name printed in blue is among the top 10 hub genes that are significantly dysregulated.

https://doi.org/10.1021/acsomega.3c00441
ACS Omega 2023, 8, 10565−10590

(A) Correlation Analysis of 10 HUB Molecular Signatures with GBM Tumor Microenvironment

Gene Name	Variable	Purity	B Cell	CD8+ T Cell	CD4+ T Cell	Macrophage	Neutrophil	Dendritic Cell
BRCA1	partial.correlation	0.312	-0.132	0.042	0.090	0.048	0.149	0.090
	p-value	0.000	0.007	0.396	0.066	0.327	0.002	0.065
CCNB1	partial.correlation	0.347	-0.069	0.011	-0.161	-0.069	-0.038	0.070
	p-value	0.000	0.159	0.823	0.001	0.161	0.441	0.154
CDC20	partial.correlation	0.413	-0.135	-0.056	-0.091	-0.073	-0.086	0.054
	p-value	0.000	0.006	0.257	0.062	0.136	0.078	0.267
EXO1	partial.correlation	0.487	-0.067	-0.059	-0.072	-0.052	-0.054	-0.022
	p-value	0.000	0.174	0.225	0.141	0.293	0.268	0.656
KIF11	partial.correlation	0.404	-0.098	-0.018	0.004	-0.008	0.058	0.073
	p-value	0.000	0.046	0.721	0.932	0.863	0.234	0.138
LYN	partial.correlation	-0.439	0.277	-0.358	0.232	0.241	0.399	0.500
	p-value	0.000	0.000	0.000	0.000	0.000	0.000	0.000
MMP9	partial.correlation	-0.173	-0.095	-0.186	-0.059	-0.086	0.037	0.333
	p-value	0.000	0.052	0.000	0.228	0.079	0.449	0.000
PCNA	partial.correlation	0.382	0.061	0.054	-0.108	-0.016	-0.028	0.077
	p-value	0.000	0.211	0.267	0.027	0.750	0.564	0.117
PSMB9	partial.correlation	-0.172	0.324	-0.214	-0.031	0.099	0.153	0.229
	p-value	0.000	0.000	0.000	0.527	0.042	0.002	0.000
TIMP1	partial.correlation	-0.392	-0.119	0.002	0.009	0.050	-0.120	0.547
	p-value	0.000	0.015	0.975	0.847	0.310	0.014	0.000

Spearman positive correlation (ρ>0, p<0.05) Spearman negative correlation (ρ<0, p<0.05)

(B) Correlation Of 4 Molecular Signatures With Immune Infiltration in GBM

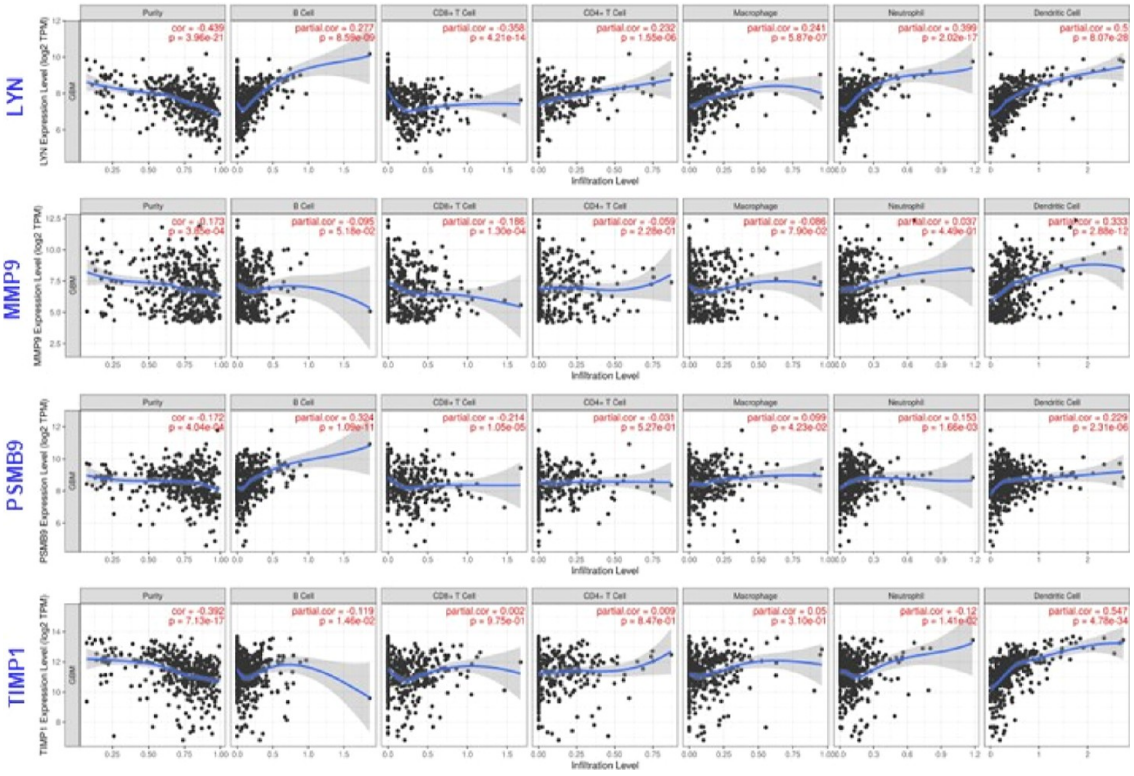

Figure 3. (A) Correlation analysis of 10 validated hub genes in GBM patient's data sets with tumor purity and six tumor infiltrating immune cells (B-cells, CD8+ T cells, CD4+ T cells, macrophages, neutrophiles, and DCs). Genes highlighted in blue show negative tumor purity and hence shortlisted for further analysis. (B) Scatterplots from the TCGA-GBM data set illustrating the relationship between LYN, MMP9, PSMB9, and TIMP1 gene expressions and tumor purity and six key tumor infiltrating immune cell types in GBM. On the left-most panel, gene expression levels are compared to tumor purity, and genes that are highly expressed in the microenvironment are expected to have negative associations with tumor purity. In the TIMER database analysis, partial Spearman's correlation was applied. When $|\rho| > 0.1$ and p-value ≤ 0.05, it indicated that there was a link between the genes and immune cells. In general, the smaller the ρ value, the smoother the curve; the larger the ρ value, the fuller the curve; when $\rho < 0.5$, the curve is ellipse; when $\rho = 0.5$, the curve is parabola; when $\rho \geq 0.5$, the curve is hyperbola.

https://doi.org/10.1021/acsomega.3c00441
ACS Omega 2023, 8, 10565−10590

integrated the 3 enrichment analysis methods, a total of 241 GBM-related DEGs were documented, including 129 upregulated genes and 112 downregulated genes (Supporting Information Table S1).

3.2. PPI Analysis and Exploration of HUB Signatures in Hypoxia-Induced GBM. With the help of the STRING database on Cytoscape software, we evaluated the PPI network comprising 241 DEGs based on coexpression to explore the possibility of hub genes. The network consists of 163 nodes and 592 edges with a high confidence score of ≥0.700. Molecular signatures in the network were displayed based on their expression (green for upregulation, red for downregulation) and intensity based on fold change (log fold change, value: −6 to +14). To evaluate the importance of nodes in the PPI network, the topological parameters, including degree centrality and betweenness centrality, were calculated and utilized in the present study using the CentiScaPe plugin in Cytoscape software to find hub genes. We observed degree with a range of 1−14 and betweenness with a range of 0−684. Using the online Venny 2.0 tool, we observed the exchange and generated a Venn plot between "degree" and "betweenness" (Figure 1B,b). The 32 hub genes, a small number of critical nodes for the protein interactions in the PPI network, were chosen with a degree centrality > 7.00 (average value) and betweenness centrality > 342 (average value). PPI networks for DEGs and hub genes are shown in Figure 2A,B, respectively.

3.3. Validation of HUB Signatures in GBM Patients. We conducted the expression analysis of all 32 HUB signatures using various online web servers for RNA sequencing data, such as GEPIA2.0, TIMER2.0, TCGA-GBM, and GlioVis-GILL, and microarray data, such as GlioVis-REMBRAND, GlioVis-AGILENT, and GlioVis-Gravendeel. These web servers from the TCGA project provide extensive information concerning GBM patients. The expression of all 32 genes was examined using the databases described above as described in Table 1. Based on the selection criteria (***$p \leq 0.001$; **$p \leq 0.01$; *$p \leq 0.05$; ns, not significant), 10 genes out of 32 exhibited significant expression levels in both RNA and microarray databases of GBM patient samples. This also explains that these 10 molecular signatures, namel,y BRCA1, CCNB1, CDC20, EXO1, KIF11, LYN, MMP9, PCNA, PSMB9, and TIMP1, were expressed in GBM tumor samples. Molecular function of these signatures and their role in various malignancies have been briefly explained here. Breast cancer gene 1 (BRCA1) is a tumor suppressor protein that is essential for DNA damage repair, chromatin remodeling, and cell cycle regulation. Mutations in BRCA1 cause genetic changes, cancer, and a failure to repair DNA damage. Patients with BRCA1 germ line mutations have been associated with sporadic instances of GBM.[67] Cyclin B1 (CCNB1) and cell division cycle protein 20 (CDC20), both of which are associated with cell progression, demonstrated that their increased expression was substantially correlated with poor survival in GBM.[68] Exonuclease 1 (EXO1) is a member of the DNA damage repair enzyme family that is particularly active in homologous recombination (HR) and nonhomologous end-joining following DNA double-strand breaks. It increases cell proliferation, invasion, and metastasis in glioma and hepatocellular carcinoma.[69] According to Liu et al., increased Kinesin family member 11 (KIF11) enhances cell cycle development and chemoresistance, negatively correlates with the TP53 expression, and is a major cause of malignancy in GBM.[70] Lck/yes-related protein tyrosine kinase (LYN) showed a substantial positive connection with PD-L1, was connected to the control of carcinogenic genes, and was engaged in tumor mutation. In gliomas, LYN may serve as both a potential diagnostic and immunotherapy marker.[71] Likewise, the proliferative capacity of cells is impacted by high MMP9 expression in gliomas, which is also linked to patient survival rates.[72] Proteasome 20S subunit beta 9 (PSMB9), along with PSMB8 and PSMB10 genes that encode catalytic subunits of the immunoproteasome, was overexpressed in GBM and was reported by Liu et al. as a novel biomarker for lower-grade glioma prognosis and can be exploited as an immunotherapy target.[73] Similarly, a study by Smith et al., demonstrated that proliferating cell nuclear antigen (PCNA), a nuclear DNA replication and repair protein, has increased expression and poor prognosis in pancreatic ductal adenocarcinoma.[74] Last but not least, tissue inhibitor of metalloproteinases-1 (TIMP-1) is known to control the proteolytic activity of the MMPs that break down the extracellular matrix. High tumor TIMP-1 protein expression in GBM has been linked to irinotecan resistance and anticipated to predict lower overall survival in GBM.[75]

Thus, only 10 molecular signatures were selected for further analysis, which were significantly expressed in all seven patient GBM databases.

3.4. Correlation between HUB Signatures and GBM TME. Here, in this study, to filter out molecular signatures involved in TME, we used the TIMER database to investigate the connection and correlation of 10 molecular signatures (BRCA1, CCNB1, CDC20, EXO1, KIF11, LYN, MMP9, PCNA, PSMB9, and TIMP1) expression with tumor purity and immune cell infiltration in patients with hypoxia-induced GBM. Data have been compiled in Figure 3A. In addition, we used GBM data sets to estimate the amounts of infiltration of six immune cell types [(CD4+ T cells, CD8+ T cells, B cells, macrophages, neutrophils, and DCs). Tumor purity normalized spearman correlation analyses revealed a positive and negative correlation expression of hub genes with B cells, CD4+ T cells, CD8+ T cells, macrophages, neutrophils, and DCs in GBM cancer. After the inputs are successfully entered, scatterplots will be created and displayed, displaying the purity-corrected partial Spearman's rho value (ρ) and statistical significance. Genes with negative associations with tumor purity are highly expressed in TME, and positive associations are highly expressed in the tumor cells. Finally, we discovered four molecular signatures (LYN, MMP9, PSMB1, and TIMP1) with negative tumor purity, and it implicated in the GBM's hypoxic microenvironment. Figure 3B illustrates the scatterplot showing the relationship between LYN, MMP9, PSMB9, and TIMP1 gene expressions and tumor purity and six key tumor-infiltrating immune cell types in GBM.

LYN expression shown positive correlation with B cells (ρ = 0.28, $p < 0.001$), CD8+ T cells (ρ = 0.23, $p < 0.001$), macrophages (ρ = 0.24, $p < 0.001$), neutrophils (ρ = 0.39, $p < 0.001$), and DCs (ρ = 0.49, $p < 0.001$) and negative correlation with $CD8^+$ T Cells (ρ = −0.35, $p < 0.001$) in GBM. MMP9 shows positive correlation with DCs (ρ = 0.33, $p < 0.001$) and negative correlation with CD8+ T Cells (ρ = −0.18, $p < 0.001$). PSMB9 showed positive correlation with B cells (ρ = 0.32, $p < 0.001$), macrophages (ρ = 0.99, $p < 0.001$), neutrophils (ρ = 0.15, $p < 0.001$), and DCs (ρ = 0.22, $p < 0.001$) and negative correlation with $CD8^+$ T Cells (ρ = −0.21, $p < 0.001$).

A study by Wang et al., showed that cancer-derived MMP9 plays a crucial role in the development of tolerogenic DCs which further affects regulatory T cells (T_{reg}) in the case of laryngeal cancer.[76] Similarly, mounting evidence suggested that MMP9

https://doi.org/10.1021/acsomega.3c00441
ACS Omega 2023, 8, 10565−10590

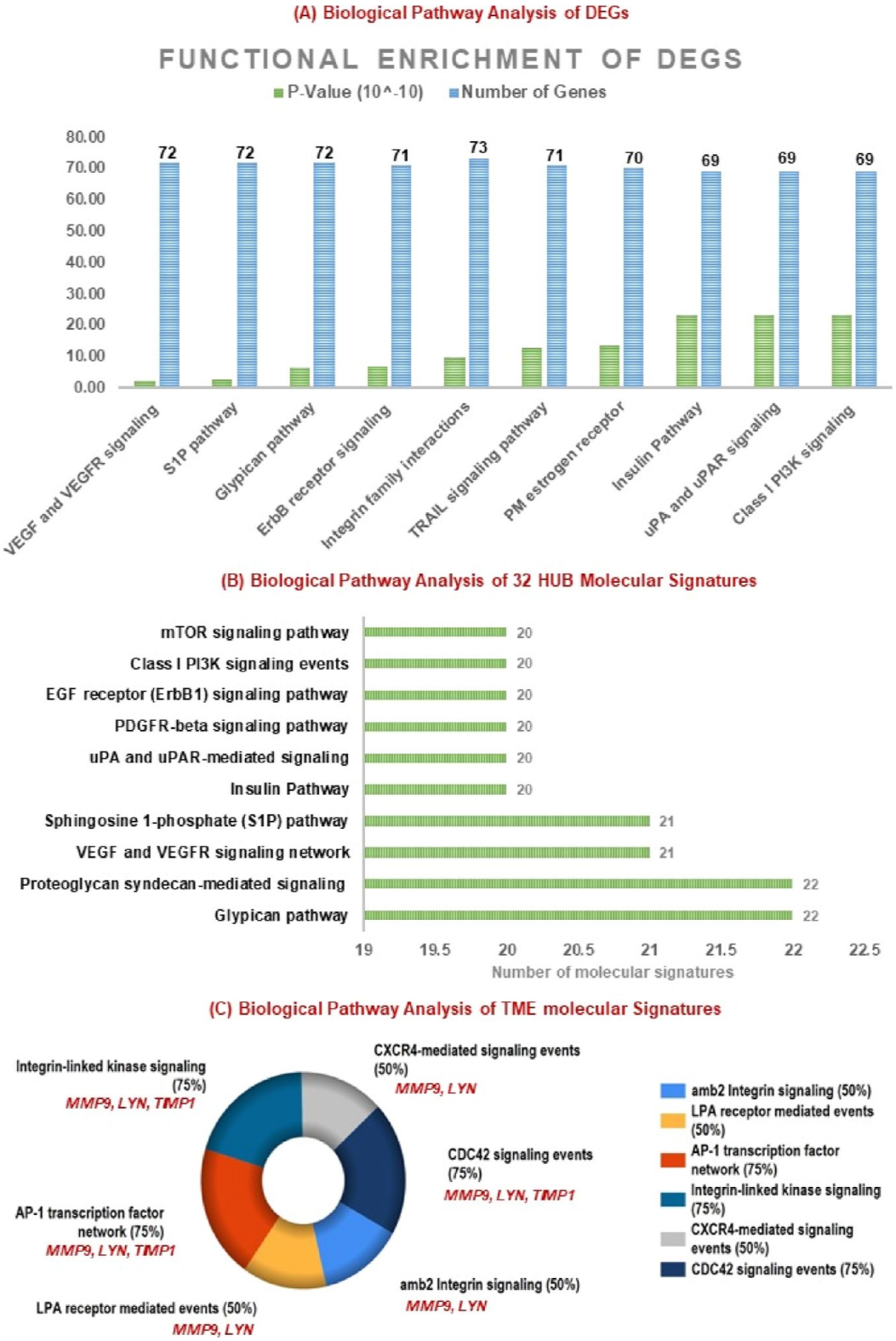

Figure 4. Significantly enriched biological pathway analysis: (A) Top 10 significantly functional enriched biological pathway terms of 241 DEGs associated with hypoxia-GBM. (B) Top 10 significantly functional enriched biological pathway terms of 32 hub signatures associated with hypoxia-GBM. (C) Top six enriched pathways of four molecular signatures (LYN, MMP9, PSMB9, and TIMP1) linked with the GBM microenvironment. Functional and signaling pathway enrichments were conducted using the KEGG pathway (http://www.genome.jp/kegg) and FunRich tool.

was involved in cancer-related inflammation by proteolyzing extracellular signal proteins, primarily those belonging to the CXC (C-X-C motif) chemokine family. As a result, MMP9 is regarded as a key architect and organizer of the tumor immune microenvironment.[77] Last TIMP1 expression linked positively with DCs ($\rho = 0.54$, $p < 0.001$) and negatively with B cells ($\rho = -0.11$, $p < 0.001$) and neutrophils ($\rho = -0.11$, $p < 0.001$). In contrast, BRCA1, CCNB1, CDC20, EXO1, KIF11, and PCNA

https://doi.org/10.1021/acsomega.3c00441
ACS Omega 2023, 8, 10565−10590

showed positive correlations with tumor purity, attributed to their predominant expression and functions in tumor cells. Further, we identified the relationship between somatic cell number alteration and the presence of immune infiltrates of four genes (Supporting Information Figure S2A). Additionally, we have examined the connection between these molecular signatures and immune checkpoint inhibitors (ICIs), including PDCD1(PD1), CD274(PDL1), CTLA4, LAG-3, and HAVCR2(TIM-3) (Supporting Information Figure S2B). According to data, the genes LYN, PSMB9, and TIMP1 were all positively correlated with ICIs except for LAG3, while TIMP1 was negatively correlated with LAG3. MMP9 only had positive correlation with PD1 and TIM-3.

Therefore, we have discovered four molecular signatures, LYN, MMP9, PSMB9, and TIMP1, to target the microenvironment of GBM and to further research whether they are therapeutic targets or not. The study concluded that LYN and PSMB9 were downregulated in hypoxia-induced GBM with $\log_2$ fold change values of −2.247 and −2.096, whereas MMP9 and TIMP1 were upregulated with $\log_2$ fold change values of 2.144 and 1.647, respectively. Thus, TIPM1 and MMP9 were selected for the identification of novel natural compounds in hypoxia-induced GBM therapeutics. However, TIMP1 lacks the approved control drug in terms of chemical compound and hence discarded for further analysis. Thus, the current study aims to identify the novel natural compound against MMP9 in hypoxia-induced GBM.

3.5. Biological Pathway Analysis of DEGs, HUB Molecular Signatures, and TME-Related Signatures. Biological pathway analysis using FunRich software was performed on 241 DEGs, 32 hub genes, and 4 genes involved in TME. As shown in Figure 4A, DEGs involved in the top 10 significant biological pathways were (a) VEGF and VEGFR signaling, (b) sphingosine 1-phosphate (S1P) pathways, (c) glypican pathway, (d) ErbB receptor signaling pathway, (e) integrin family cell surface interactions, (f) TRAIL signaling pathway, (g) plasma membrane estrogen receptor signaling, (h) insulin Pathway, (i) urokinase-type plasminogen activator (uPA) and uPAR-mediated signaling, and (j) class I phosphatidylinositol-3-kinase (PI3K) signaling. Similarly, analysis of 32 hub genes enhanced in biological pathways were (Figure 4B) (a) glypican pathway, (b) proteoglycan syndecan-mediated signaling, (c) VEGF and VEGFR signaling, (d) S1P pathway, (e) insulin pathway, (f) uPA and uPAR-mediated signaling, (g) PDGFR-beta signaling, (h) ErbB1 signaling pathway, (i) class I PI3K signaling, and (j) mTOR signaling pathway. In addition, we have also analyzed four shortlisted molecular signatures involved in TME in Figure 4C to understand the major pathways involved, which were (a) integrin-linked kinase (ILK) signaling, (b) activating protein-1 (AP-1) transcription factor network, (c) CDC42 signaling events, (d) CXCR4-mediated signaling, (e) Amb2 integrin signaling, and (f) lysophosphatidic acid (LPA) receptor-mediated. Biological pathways with p-value ≤ 0.05 and count > 2 were measured as statistically significant.

3.6. Localization Study and Construction of Target Signature−Regulatory Transcription Factor Network. Based on the CELLO localization predictor, we have predicted the localization of four genes using their amino acid protein sequences. Results showed that MMP9 and TIMP1 were majorly localized in the extracellular space, followed by the plasma membrane. At the same time, LYN and PSMB9 were localized in the cytoplasm and chloroplast, respectively (Supporting Information Figure S3A). Further, we have predicted target genes (LYN, PSMB9, MMP9, and TIMP1) related to TFs and their expression in GBM patient samples using JASPAR and GEPIA2.0 databases, respectively. The main transcription factor and its targets are listed in (Supporting Information Figure S3B.1). TIMP1, MMP9, and PSMB9 all share the Yin Yang 1 (YY1) TF with the highest degree (3) and betweenness (109.00), but the expression in the GBM patient sample is not statistically significant. In contrast, TIMP1 and PSMB9 shared the RELA (degree: 2; betweenness: 33.83), but TFAP2A and NFKB1 were elevated against PSMB9 with $\log_2$ fold change ≥ 1.4 (p-value ≤ 0.05) in GBM. However, TFs against the MMP9 gene were FOS, JUN, and TP53. These TFs were upregulated in GBM ($\log_2$ fold change ≥ 1.5, p-value ≤ 0.05), whereas STAT3 was only upregulated TF against the LYN gene. Supporting Information Figure S3B.2 demonstrates the network showing the associated transcription factor with molecular signatures in GBM.

3.7. Screening of Natural Compounds Based on BBB and ADMET Analyses. We received plant-derived naturals compounds from the NPACT database, including terpenoids, flavonoids, alkaloids, polycyclic aromatic natural compounds, aliphatic natural compounds, tannin, and PubMed database. We carried out BBB permeability of all-natural compounds using the SwissADME and CBLigand online tool with a cutoff value of 0.02 as we know that protein associated with GBM will be found in the particular region of the brain; thus, for a drug to be effective, it must pass the BBB.[78] In addition, these were checked for positive DLS based on drug-likeness score prediction.[79] Also, compounds were studied for Lipinski rule (MW ≤ 500; log P ≤ 5; HBA ≤ 10; HBD ≤ 5) and PAINS alert.[80] Sixty-five novel natural compounds had passed the criteria of BBB, Lipinski rule, PAINS, and drug-likeness, which went under ADMET (absorption, distribution, metabolism, excretion, and toxicity) analysis.[81] ADMET analysis of nominated compounds was carried out to check the pharmacokinetics and pharmacodynamics properties. This server was selected to assess whether a ligand (drug) is hepatotoxic, nephrotoxic, arrhythmogenic, carcinogenic, or respiratory toxic because poor pharmacokinetics and toxicity of candidate compounds are the significant reasons for drug development failure. Our study predicts 18 ADMET properties of selected compounds out of the 3 of absorption, 2 of distribution and excretion, 1 of metabolism, and 10 of toxicity properties.

For each compound to be an effective drug, it must fulfill these parameters which have their own range values such as (a) *Absorption*: Caco2 permeability > −5.15 log cm/s, MDCK permeability (Papp) > 20×10^{-6} cm/s, intestinal absorption > 30%; (b) *Distribution*: plasma protein binding ≤ 90%, volume distributionVD: 0.04−20 L/kg; (c) *Metabolism*: CYP1A2 inhibitor a cytochrome P450 enzymes. Inhibitors of CYP1A2 will boost the medication's plasma concentrations, and in some situations, this will result in negative consequences;[82] (d) *Excretion*: clearance of a drug ≥ 5, the half-life of a drug ($T_{1/2}$): 0−0.3; (e) *Toxicology*: human ether-a-go-go related gene (hERG blockers), human hepatotoxicity (H-HT), Drug-induced liver injury, AMES Toxicity, Rat Oral Acute Toxicity, toxic dose threshold of chemicals in humans (FDAMDD), skin sensitization, carcinogenicity, eye corrosion/irritation, and respiratory toxicity range between 0 and 0.3 (—): excellent (green); 0.3−0.7 (+)/(−): medium (yellow); 0.7−1.0 (++): poor (red).

https://doi.org/10.1021/acsomega.3c00441
ACS Omega 2023, 8, 10565−10590

Table 2. List of Identified 11 Natural Compounds and Their Toxicity Profiles[a]

PubChem CID	158280	185609	10424988	13886678	44479222	15549893	124256	162334	1548943	101477139	14313693
Natural Compounds	7,4'-dihydroxyflavan	4'-hydroxy-7-methoxyflavan	4,4'-dihydroxy-2,6-dimethoxydihydrochalcone	7-Hydroxy-2',4'-dimethoxyisoflavanone	(3R)-3-(4-Hydroxybenzyl)-6-hydroxy-8-methoxy-3,4-dihydro-2H-1-benzopyran	4'-hydroxy-2,4-dimethoxydihydrochalcone	N-(4-hydroxyundecanoyl)anabasine	N-n-octanoylnornicotine	8-Methyl-N-Vanillyl-6-Nonenamide	Multidione	Naviculol
Molecular formula	C15H14O3	C16H16O3	C17H18O5	C17H16O5	C17H18O4	C17H18O4	C21H34N2O2	C17H26N2O	C18H27NO3	C20H28O3	C15H26O
hERG Blockers	(---)	(--)	(---)	(---)	(--)	(--)	(---)	(---)	(---)	(---)	(---)
H-HT	(---)	(---)	(---)	(--)	(--)	(--)	(+)	(-)	(--)	(--)	(---)
DILI	(---)	(--)	(--)	(+)	(---)	(+)	(---)	(---)	(---)	(--)	(---)
AMES Toxicity	(-)	(+)	(---)	(+)	(---)	(--)	(---)	(---)	(---)	(---)	(---)
Rat Oral Acute Toxicity	(--)	(--)	(--)	(--)	(---)	(--)	(---)	(---)	(---)	(---)	(---)
FDAMDD	(+)	(+)	(-)	(+)	(++)	(-)	(+++)	(++)	(---)	(--)	(---)
Carcinogencity	(+)	(+)	(--)	(-)	(+)	(+)	(---)	(---)	(---)	(---)	(++)
Eye Corrosion	(+)	(---)	(---)	(---)	(---)	(---)	(---)	(---)	(---)	(---)	(---)
Eye Irritation	(+++)	(+++)	(+)	(---)	(++)	(++)	(---)	(---)	(---)	(+)	(+)
Respiratory Toxicity	(--)	(--)	(--)	(--)	(--)	(--)	(---)	(--)	(---)	(--)	(+)
Caco2 permeability (> -5.15log cm/s)	-4.691	-4.7	-4.695	-4.796	-4.663	-4.747	-4.68	-4.494	-4.476	-4.657	-4.205
MDCK Permeability (> 20X10-6 cm/s)	1.10E-05	1.40E-05	1.70E-05	3.40E-05	1.60E-05	2.10E-05	2.8E-05	1.90E-05	2.70E-05	2.10E-05	1.70E-05
Intestinal absorption	(---)	(---)	(---)	(---)	(---)	(---)	(---)	(---)	(---)	(---)	(---)
PPB (≤ 90%)	96.63%	97.48%	86.48%	98.13%	96.01%	91.47%	88.48%	86.43%	96.49%	98.34%	95.56%
VD (0.04-20L/kg)	1.111	1.194	0.595	0.55	1.044	0.574	0.956	0.867	1.098	0.316	1.553
CYP1A2 inhibitor	(+++)	(+++)	(+++)	(+++)	(+++)	(+++)	(---)	(-)	(++)	(-)	(--)
CL(≥ 5)	16.437	12.53	11.71	9.771	14.822	12.32	9.359	6.442	11.309	9.861	12.763
T1/2	0.757	0.335	0.914	0.384	0.813	0.818	0.3	0.281	0.892	0.465	0.22

[a]Color code: green/(—): signifies excellent with score range between 0 and 0.3; yellow/(+)/(−): signifies medium with score ranging between 0.3 and 0.7; red/(++/+++) signifies poor with score range between 0.7 and 1.0.

https://doi.org/10.1021/acsomega.3c00441
ACS Omega 2023, 8, 10565−10590

Papp is extensively considered to be the in vitro point of reference for estimating the uptake efficiency of compounds into the body. Papp values of MDCK cell lines were also used to estimate the effect of the BBB. hERG-(Category 0) compounds had an IC_{50} > 10 μM or <50% inhibition at 10 μM, whereas hERG + (Category 1) molecules will have the opposite of this. The voltage-gated potassium channel encoded by hERG genes plays a key function in controlling the exchange of cardiac action potential and resting potential during cardiac depolarization and repolarization. Long QT syndrome, arrhythmia, and Torsade de Pointes are all possible side effects of hERG blocking and can result in palpitations, fainting, or even death. Hepatotoxicity predicts the action of a compound on normal liver function. Furthermore, if the given compound is AMES positive, it will be considered mutagenic. Similarly, compounds have positive carcinogenicity because of their ability to damage the genome or disrupt the cellular metabolic processes. Recently, respiratory toxicity has become the leading cause of drug withdrawal. Drug-induced respiratory toxicity is frequently underdiagnosed due to the lack of recognizable early signs or symptoms in commonly used drugs, resulting in severe morbidity and mortality. As a result, thorough monitoring and treating respiratory toxicity are critical.[83,84] Our study indicates that all 11 predicted compounds, alkaloids (PubChem CID:124256, 162334, and 1548943), terpenoids (PubChem CID: 101477139 and 14313693), and flavonoids (PubChem CID: 158280, 185609, 10424988, 13886678, 44479222, and 15549893) fulfill the eligibility criteria and show favorable results. Therefore, we summarize in Table 2 that all 11 natural compounds meet the ADMET criteria for being a novel compound to target GBM. The detailed methodology used to screen natural compounds are shown in Supporting Information Figure S4, and the characteristics and physiochemical of natural compounds are mentioned in Supporting Information Table S2.

3.8. 7,4′-Dihydroxyflavan, (3*R*)-3-(4-Hydroxybenzyl)-6-hydroxy-8-methoxy-3,4-dihydro-2*H*-1-benzopyran), and 4′-Hydroxy-7-methoxyflavan) as Promising Natural Flavonoids Against MMP9: a Molecular Docking Approach. To find effective drugs against the MMP9 gene, 11 natural compounds satisfied the filter criteria, and one reference drug, Captopril (FDA approved retrieved from the DrugBank database; https://www.drugbank.ca/) and one natural compound (Solasodine) from previous studies[85,86] were chosen. Autodock Vina 4.0 was used to perform blind molecular docking experiments of all prioritized natural compounds with MMP9 (PDB id: 4HMA) using default parameters. The docking or binding free energy screens the most effective chemicals and conformations. Table 3 depicts the particular docking binding energy [$-\Delta G$ value (kcal/mol)] and the detailed information regarding intermolecular interactions between ligands and proteins. In addition, we have predicted the binding residues for ligand binding using the PrankWeb tool. Pocket 1 with highest probability (0.99) was chosen whose residues for alpha chain were 179, 180, 186−193, 222, 223, 226, 227, 230, 233−238, 240, 242, 243, and 245−249.

The MMP9 3D structure revealed that 88.6% of the residues were in the highly favored region and 0.4% were in the disallowed region respectively. Further structures were validated by ERRAT and VERIFY3D. The quality factor predicted by the ERRAT server for both alpha and beta chains of MMP9 was 76.17. VERIFY3D server predicted that 100% of residues had averaged a 3D−1D score ≥ 0.2respectively. Moreover, the docking energy of reference drugs, Captopril and Solasodine, were −6.6, −10.3 kcal/mol, respectively. Among 11 natural compounds, flavonoid 7,4′-dihydroxyflavan) and (3*R*)-3-(4-hydroxybenzyl)-6-hydroxy-8-methoxy-3,4-dihydro-2*H*-1-benzopyran) scored the highest binding energy −10.3 kcal/mol with 2 H-bond interaction with GLU241, ALA242, Leu188, and HIS226 than both the reference drugs, whereas 4′-hydroxy-7-methoxyflavan scored −10 kcal/mol binding energy with no H-bond interaction. Supporting Information Figure S5 shows two-

Table 3. Binding Affinity and Binding Energy of Prioritized Natural Compounds along with the Reference Drug

Group	Reference Drug		Experimental Natural Compounds										
PubChem CID	*442985*	*44093*	*158280*	*44479222*	*185609*	*13886678*	*10147739*	*10424988*	*124256*	*15549893*	*1548943*	*162334*	*14313693*
Class of compounds	*Alkaloid*	*Small molecules*	*Flavonoid*	*Flavonoid*	*Flavonoid*	*Flavonoid*	*Terpenoid*	*Flavonoid*	*Alkaloid*	*Flavonoid*	*Alkaloid*	*Alkaloid*	*Terpenoid*
Ligand Name	Solasodine	Captopril	7,4′-dihydroxyflavan	(3R)-3-(4-Hydroxybenzyl)-6-hydroxy-8-methoxy-3,4-dihydro-2H-1-benzopyran	4′-hydroxy-7-methoxyflavan	7-Hydroxy-2′,4′-dimethoxyisoflavanone	Multidione	4,4′-dihydroxy-2,6-dimethoxydihydrochalcone	N-(4-hydroxyundecanoyl)anabasine	4′-hydroxy-2,4-dimethoxydihydrochalcone	8-Methyl-N-Vanillyl-6-Nonenamide	N-n-octanoylnornicotine	Naviculol
Total No. of interactions	15	14	17	17	16	16	17	16	22	15	17	14	9
No of interaction with active site residues	15	11	15	14	13	15	16	15	19	14	14	13	4
Binding Energy (kcal/mol)	-10.3	-6.6	-10.3	-10.3	-10	-8.5	-8.2	-8.2	-8.2	-8.2	-8.1	-7.1	-6.4
Conventional H-bond	HIS226	-	GLU241; ALA242	LEU188; HIS226	-	-	TYR248	HIS226	-	HIS226; GLN227; HIS236	GLN227; ARG249	TYR248	-
Carbon H-bond	-	ALA242	-	-	-	ALA189; HIS226	-	-	-	-	TYR245	PRO246	-
Van der waals	GLY186; ALA189; HIS190; ALA191; GLN227; HIS230; PRO246; MET247;	LEU188; VAL223; PRO249; GLU241; TYR245; MET247; ARG249; THR251	LEU188; HIS230; HIS236; PRO240; TYR245 PRO246; MET247; TYR251	ALA189; GLN227; GLU241; ALA242; TYR245; MET247; TYR248; ARG249; THR251; HIS257	HIS257; THR251; ALA242; LEU222; LEU188; GLN227; PRO246; MET247; TYR245; GLU241	LEU222; VAL223; GLN227; HIS236; LEU243; TYR245 PRO246 MET247; TYR248; ARG249; THR251	ALA189; GLY186; LEU188; TYR218; LEU222; GLN227; ALA242; TYR245; PRO246; MET247; ARG249; HIS236	GLY186; LEU187; LEU222; VAL223; GLN227; LEU243; TYR245; PRO246; ARG249; THR251	GLY186; LEU187; ALA189; HIS190 ALA191; GLN227 GLU241; ALA242; TYR245; PRO246; MET247; ARG249; THR251	ALA189; LEU243; TYR245; MET247; TYR248; ARG249; THR251	ALA189; HIS230; GLU241; PRO246; MET247 TYR248; THR251; HIS257	GLY186; LEU187; ALA189; GLN227; HIS236; TYR245; LEU243; MET247;	GLY233; ASN262; GLY263; LEU267
Alkyl/Pi-alkyl	TYR179; LEU187; LEU188; VAL223; HIS226; HIS236; TYR248	LEU222; PRO225; LEU243	LEU222; VAL223; HIS226; LEU243; TYR248; ARG249	LEU222; VAL223; HIS226 ; PRO246	VAL223; HIS236; LEU243; TYR248; ARG249;	LEU187; LEU188;	LEU187; VAL223; HIS; 226; LEU243	LEU188; HIS226; HIS230; HIS236; MET247	LEU188; LEU222; VAL223; HIS226; HIS230; HIS236; LEU243; TYR248; PRO255	LEU188; LEU222; HIS226; HIS230; HIS236; PRO246	LEU188; LEU222; VAL223; HIS236; LEU243; ARG249	LEU188; TYR218; VAL223 HIS226	PHE110; LEU234; HIS266
Pi cation	-	-	HIS226	-	HIS226	-	HIS226		-	-	HIS226	-	-
Pi-Pi Stacked	-	-	-	HIS226	-	HIS226	TYR248	TYR248	-	HIS226		-	-
Pi-sigma	HIS226	-	-	LEU188; LEU243	-	-	-	-	-	-	-	-	-
Pi-sulphur		HIS226 ; TYR248	-	-	-	-	-	-	-	-		-	-
Unfavorable donor-donor	-	-	GLN227	-	-	-	-	-	-	-	LEU188	-	ASP235

https://doi.org/10.1021/acsomega.3c00441
ACS Omega 2023, 8, 10565−10590

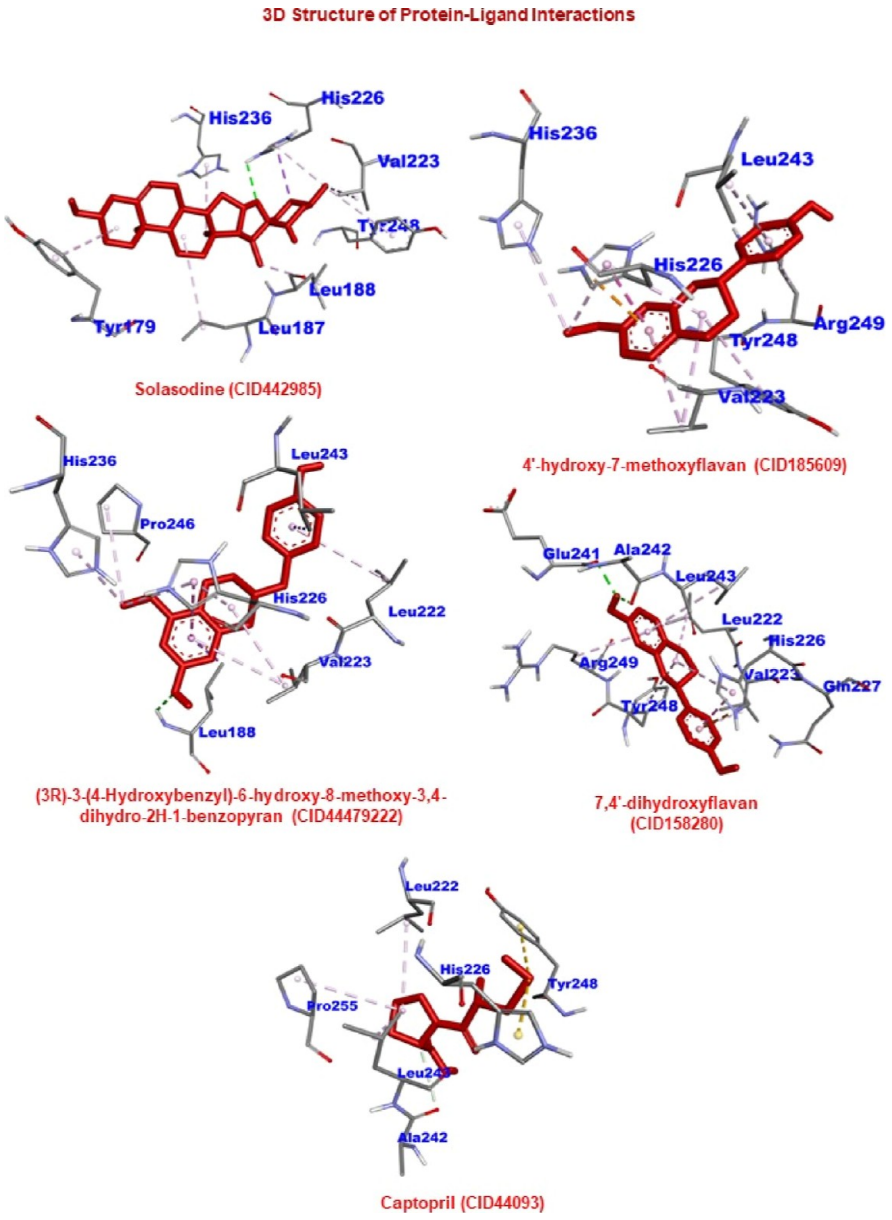

Figure 5. 3D interaction diagrams for the docked complexes between MMP9 and ligands obtained in this study.

dimensional (2D) interaction diagrams for the docked complexes between MMP9 and ligand which includes all interactions such as H-bond and other interactions such as the van der waals force, π-alkyl, π-sigma, and so forth. Shortlisted natural compounds' binding energy and H-bond interaction have been tabulated in detail in Table 3. Three natural compounds 7,4′-dihydroxyflavan and (3*R*)-3-(4-hydroxybenzyl)-6-hydroxy-8-methoxy-3,4-dihydro-2*H*-1-benzopyran), and 4′-hydroxy-7-methoxyflavan) scoring the lowest binding energy and forming interaction with the active site were shortlisted for further studies along with Captopril and Solasodine. It was intriguing to note that all best-identified natural compounds showed stable and conserved intermolecular interactions as demonstrated in Figure 5.

3.9. Assessment of the Most Promising Protein−Ligand Complex by MD Simulation Run. MD simulation (RMSD, RMSF, R_g, and SASA) results of all mentioned protein−ligand complexes have been mentioned in Figure 6 along with the average score values of each parameter of three best-docked compounds and two reference drugs.

3.9.1. Stability of MMP9-7,4′-Dihydroxyflavan Complex. The time evolution of the RMSD was determined to check the structural stability of the protein in complex ligands during the simulation. The average RMSD values for the backbone and complex were ∼2.06 and ∼2.62 Å, respectively. The complex slightly deviated as RMSD > ∼3 Å between 19 and 24 ns. At the binding site, a loop formed by the residues Pro240 and Arg249 that connects two helices displayed only slight residual fluctuations up to 0.9 Å. Flexible loops in the N-terminal region of the protein were extremely dynamic and exhibited RMSF > 2.5 Å. It was intriguing to observe that residues actively contributed to the stable interaction and exhibited significantly less fluctuation. The complex's overall average RMSF value was ∼1.13 Å. The R_g value was determined for investigating the compactness and structural changes in the MMP9-7,4′-dihydroxyflavan complex. The root-mean-square distance of a protein atom in relation to the protein's center of mass is used to

https://doi.org/10.1021/acsomega.3c00441
ACS Omega 2023, 8, 10565−10590

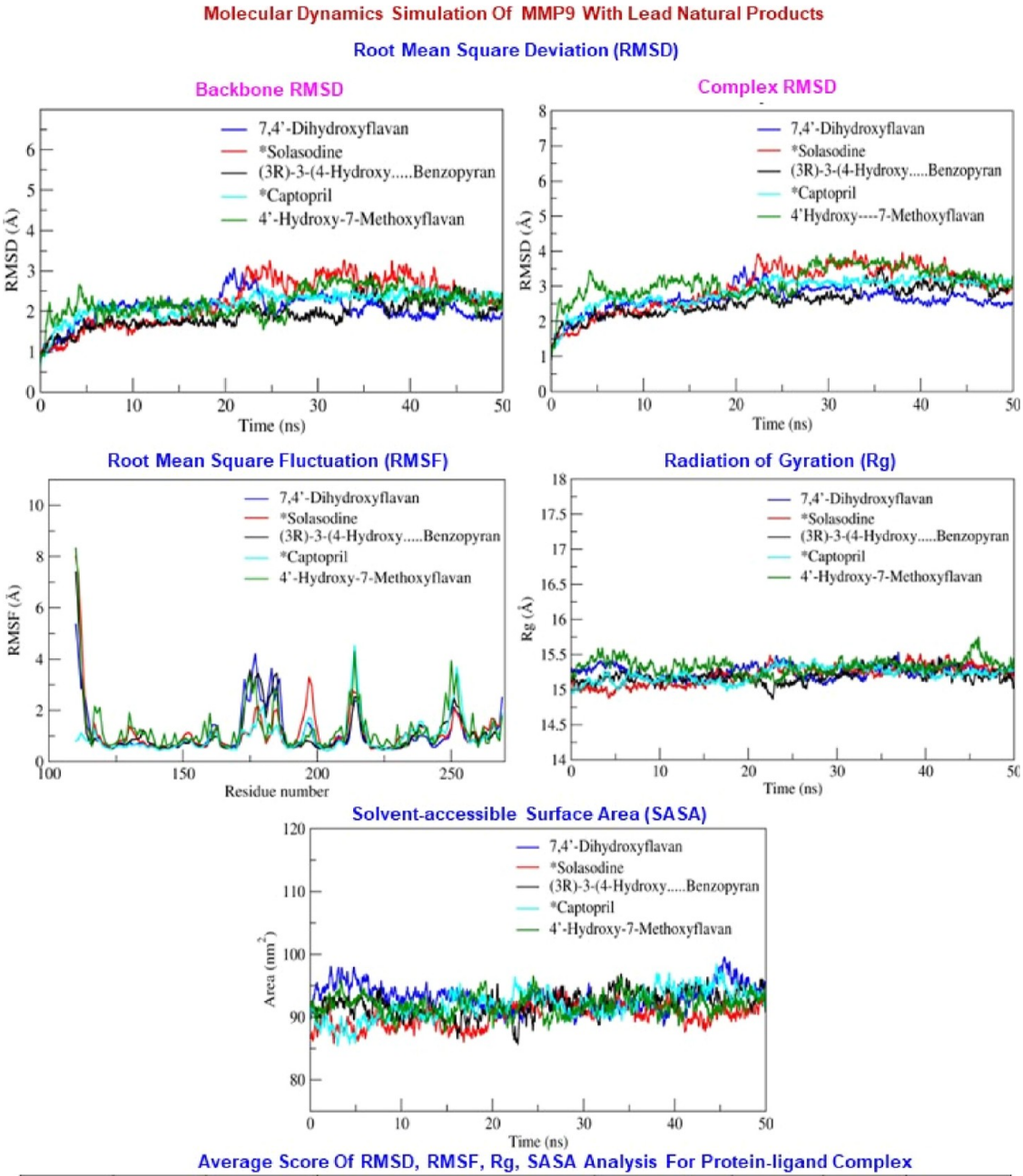

Average Score Of RMSD, RMSF, Rg, SASA Analysis For Protein-ligand Complex

Color Code	Category	PubChem CID	Ligand Name	RMSD (Å)		RMSF(Å)	Rg (Å)	SASA (nm^2)
				Backbone	Complex			
	Experimental	158280	7,4'-dihydroxyflavan	2.06	2.62	1.13	15.25	91.88
	Reference	442985	Solasodine	2.26	2.94	1.16	15.2	91.98
	Experimental	44479222	(3R)-3-(4-Hydroxybenzyl)-6-hydroxy-8-methoxy-3,4-dihydro-2H-1-benzopyran	1.91	2.58	1.13	15.18	92.15
	Reference	44093	Captopril	2.18	2.81	0.99	15.21	90.18
	Experimental	185609	4'-hydroxy-7-methoxyflavan	2.22	3.13	1.32	15.32	93.17

Figure 6. MD simulation analysis of MMP9 upon binding of the ligand as a function of time throughout 50 ns. Graph showing RMSD, RMSF, radius of gyration (R_g), and SASA for MMP9 with three best-docked compounds and two reference drugs.

compute the R_g value of the protein. The average value of R_g for the complex is ~15.25 Å. The SASA was examined to study the protein compactness behavior. The initial and final surface areas occupied by the docked MMP9-7,4′-dihydroxyflavan complex are 91.40 and 92.90 nm^2, respectively, with an average surface area of ~91.88 nm^2. This complex constructed two stable H-bonds, and both remained stagnant over the course of the simulations. The stable H-bond interactions were thought to be the primary factor that encouraged the stable complex formation. In addition, according to MM-PBSA calculation, the complex also demonstrated a binding energy of −85.24 kJ/mol. Moreover, the residues that contributed the most to the binding energy were found by computing the residue decomposition energy. The analysis suggested that five residues,

https://doi.org/10.1021/acsomega.3c00441
ACS Omega 2023, 8, 10565−10590

Table 4. MM-PBSA Calculations of Top Hit Complexes' Binding Free Energy and Interaction Energies[a]

complex	MM-PBSA (kJ/mol)				
	ΔE_{VDW}	ΔE_{ELE}	ΔG_{Sol}	ΔG_{Surf}	ΔG_{bind}
MMP9-7,4′-dihydroxyflavan	−167.19 ± 7.82	−14.98 ± 4.06	111.60 ± 9.88	−14.68 ± 0.78	−85.24 ± 11.81
MMP9-Solasodine	−148.31 ± 11.20	−777.73 ± 18.62	353.45 ± 15.04	−15.55 ± 0.91	−588.15 ± 17.82
MMP9-(3*R*)-3-(4-hydroxybenzyl)-6-hydroxy-8-methoxy-3,4-dihydro-2*H*-1-benzopyran	−141.43 ± 13.78	−79.73 ± 8.29	142.50 ± 8.45	−15.49 ± 0.72	−94.16 ± 11.65
MMP9-4′-hydroxy-7-methoxyflavan	−154.50 ± 16.07	−27.86 ± 8.96	119.80 ± 20.33	−15.87 ± 0.90	−78.44 ± 16.16
MMP9 - Captopril	−83.65 ± 13.94	−622.30 ± 35.47	198.05 ± 38.01	−10.59 ± 1.54	−518.50 ± 22.39

[a]ΔE_{VDW}—van der Waal energy, ΔE_{ELE}—electrostatic energy, ΔG_{Sol}—polar solvation energy, ΔG_{Surf}—SASA energy, and ΔG_{bind}—binding energy.

namely, Leu222, Val223, Ala242, Met247, and Tyr248, contributed considerably to the creation of the stable complex. Most importantly, the residue Tyr248 showed significant contributions to the binding affinity by scoring the lowest contribution energy of −5.41 kJ/mol, followed by Leu222 (−4.71 kJ/mol), Met247 (−3.96 kJ/mol), Val223 (−2.67 kJ/mol), and Ala242 (−2.01 kJ/mol). However, residues Gln241and Pro255 did not favor the interactions.

3.9.2. Stability of MMP9-(3R)-3-(4-Hydroxybenzyl)-6-hydroxy-8-methoxy-3,4-dihydro-2H-1-benzopyran Complex. This complex showed consistent structural stability during the simulation run for the 50 ns production run. Protein backbone and complex were found to have average RMSD values of ∼1.91 and ∼2.58 Å, respectively. The complex was a little unstable as RMSD > ∼3 Å between 33 and 37 ns and 39 to 47 ns. The maximum residual fluctuations in the N-terminal residues were >3.0 Å. However, the residues at the binding site from Leu222 to His230 (helix) and residues from Ala242 to Arg249 (loop) engaged in the stable and conserved nonbonded interactions and showed significantly much fewer variations of ∼0.5 and ∼1.13 Å, respectively. The complex has an average RMSF value of 1.13 Å. The average R_g value of 15.18 Å showed stable complex formation during the MD simulation by forming a compact structure. Meanwhile, the initial and final surface areas employed by the complex were 92.17 and 93.16 nm^2, with the average SASA score of the complex being 92.15 nm^2. During the simulation, this complex created five H-bonds, of which four were stable. The estimated binding affinity of the compound to MMP9 protein was −94.16 kJ/mol. Additionally, the residues Leu188, Leu222, Val223, His226, and Tyr248 encouraged stable complex formation. Most importantly, the decreasing order of binding affinity followed Leu222, Tyr248 and His226, Val223, and Leu188 with the lowest contribution energy of −5.74, −5.08, −4.58, −4.22, and −3.40 kJ/mol, respectively. However, the interactions were not favored by the residues Gln227 and Arg249.

3.9.3. Stability of MMP9-185609 (4′-Hydroxy-7-methoxyflavan) Complexes. The complex showed similar RMSD values of 50 ns and was stable. The complex's RMSD value ranged from 0.97 to 3.39 Å, whereas the backbone's RMSD value ranged from 0.85 to 2.5 Å. According to the residual fluctuations plotted for the Cα, binding pockets encompassing residues between Leu222 and Gly229 (helix) and Ala242 and Arg249 (loop) showed the establishment of stable nonbonded contacts in residues with lower fluctuations. Residues at the N-terminal and residues adjacent to binding pockets, including Phe250 and Glu252, show higher residual fluctuation >3 Å due to increased local flexibility and ligand interaction observed during simulation. The overall average RMSF of the complex was 1.32 Å. Moreover, the R_g value demonstrated steady complex formation for 50 ns. In addition, the initial and final surface areas occupied by complexes were 91.63 and 96.49 $nm^{2,}$ with the average SASA score of complexes being 93.17 nm^2. Two of the three H-bonds the complex created during the simulated period were consistent. The compound also had a binding energy of about −78.44 kJ/mol. Furthermore, the per-residue contribution energy showed six residues from the binding pocket, Leu188, Leu222, Val223, Leu243, Met247, and Tyr248, which had a considerable impact on the creation of a stable complex. The residues Leu188, Leu222, Val223, Leu243, Met247, and Tyr248 from the binding pocket showed significant contributions to the binding affinity by scoring the least residue decomposition/contribution energy of −2.36, −4.25, −6.22, −3.44, −2.22, and −4.23 kJ/mol, respectively. Arg249 residues do not favor the interaction.

3.9.4. Stability of MMP9-Captopril and MMP9-Solasodine Complexes. MMP9-Captopril and MMP9-Solasodine complexes showed stable interaction during the simulation run. The average RMSD value of the backbone and MMP9-Captopril complex was ∼2.18 and ∼2.81 Å, whereas the RMSD value with Solasodine was ∼2.26 and ∼2.94 Å. Moreover, the average RMSF values for the MMP9-Captopril complex and MMP9 and MMP9-Solasodine were 0.99 and 1.16 Å, respectively. Solasodine causes the N-terminal to fluctuate more than 3 Å, whereas Captopril did not cause this variation. Also, MMP9-Captopril and MMP9-Solasodine complexes have average R_g values of 15.21 and 15.2 Å, respectively. Meanwhile, MMP9-Captopril's initial and final surface areas were 88.85 and 91.54 nm^2, respectively, with an average SASA score of 90.18 nm^2. Comparatively, the MMP9-Solasodine complex had initial and final surface areas of 89.94 and 93.58 nm^2, with an average SASA score of 91.98 nm^2. Moreover, out of the three H-bonds formed, only two were stable during simulation for the Captopril complex and Solasodine complex. In addition, the the binding energy of MMP9-Captopril and MMP9-Solasodine was −518.50 and −588.15 kJ/mol, respectively. Furthermore, the MMP9-Captopril complex also showed 10 residues from the binding pocket, including Asp201, Asp205, Asp206, Asp207, Glu208, Asp235, Glu241, Glu252, Asp259, and Asp260, and significantly contributed to the stable complex formation. Likewise, 12residues, Asp177, Asp182, Asp201, Asp205, Asp206, Glu208, Asp235, Glu241, Pro246, Glu252, Asp259, and Asp260, helped create the stable MMP9-Solasodine complex.

Thus, data confirmed that the binding energies of MMP9 with ligands 7,4′-dihydroxyflavan, (3*R*)-3-(4-hydroxybenzyl)-6-hydroxy-8-methoxy-3,4-dihydro-2*H*-1-benzopyran, and 4′-hydroxy-7-methoxyflavan were similar (−10 kcal/mol) to that of the reference drug Solasodine and better than Captopril. All three natural compounds interact within the binding domain of the MMP9 pocket, and this interaction was stable for 50 ns with less deviation and fluctuations. The RMSD value difference

https://doi.org/10.1021/acsomega.3c00441
ACS Omega 2023, 8, 10565−10590

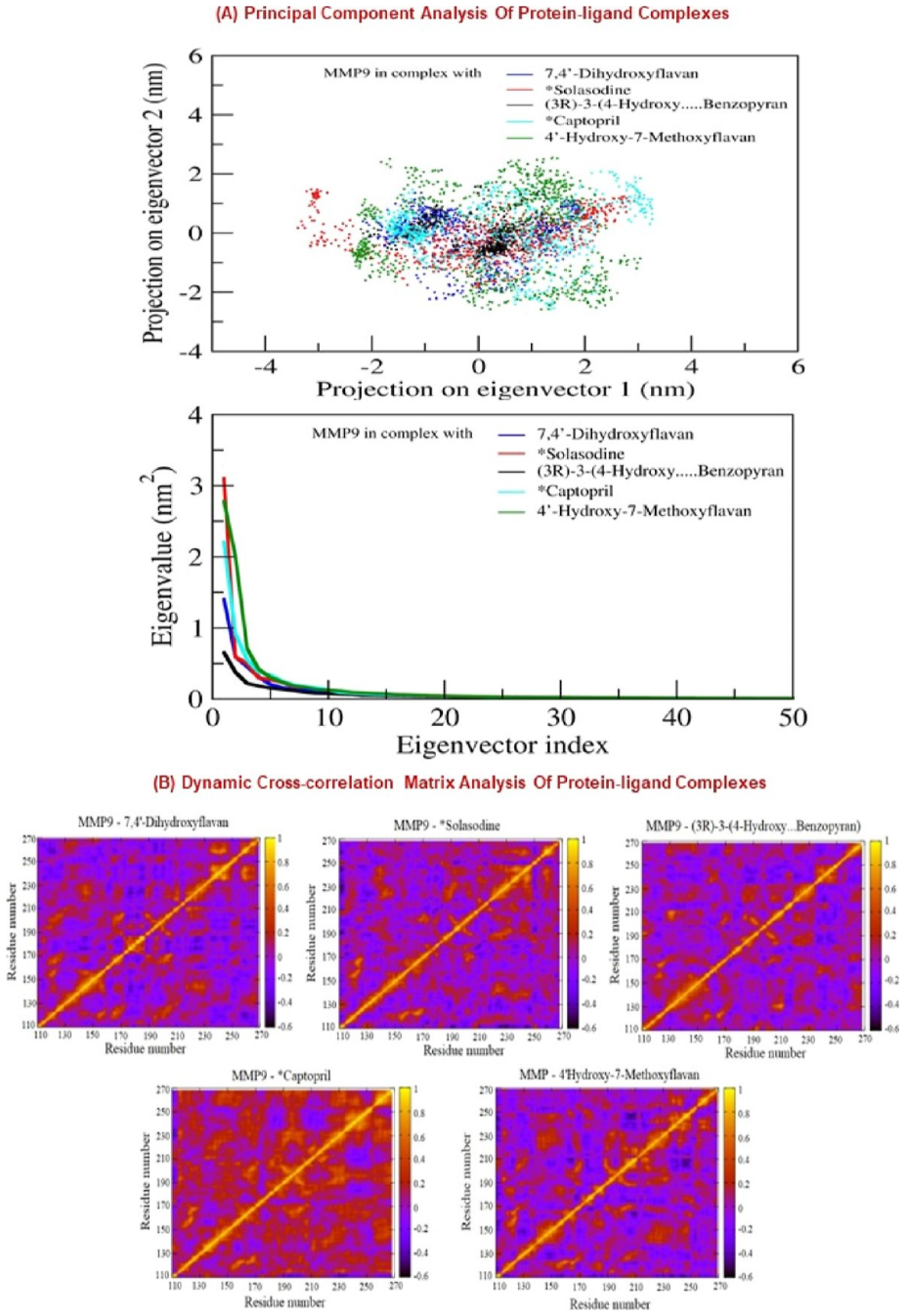

Figure 7. (A) PCA of protein−ligand complexes: In the scatterplot, the first two principal components (PC1, PC2) were plotted to analyze the collective motion of ligand-bound protein complexes during the simulations. The dots with different colors (blue, red, black, aqua, and green) represent the collective motion of MMP9 residue after ligand binding. Dots with smaller regions represent the higher structural stability and conformation flexibility and vice versa. The collective motion of MMP9 in the presence of ligands is depicted in the second graph using projections of MD trajectories onto two eigenvectors corresponding to the first two principal components. The first 50 eigenvectors were plotted versus eigenvalue for 5 ligands including 3 hit natural compounds and 2 reference drugs. Color code used in the scatterplot and graph: blue: 7,4′-dihydroxyflavan; red: Solasodine; black: (3*R*)-3-(4-hydroxybenzyl)-6-hydroxy-8-methoxy-3,4-dihydro-2*H*-1-benzopyran),;aqua: Captopril; Green: 4′-hydroxy-7-methoxy-flavan. (B) DCCM of Cα atoms observed in complexes for 7,4′-dihydroxyflavan, Solasodine, (3*R*)-3-(4-hydroxybenzyl)-6-hydroxy-8-methoxy-3,4-dihydro-2*H*-1-benzopyran), Captopril, and 4′-hydroxy-7-methoxyflavan. The positive regions, colored amber, represent strongly correlated motions of Cα atoms (C_{ij} = 1), whereas the negative regions, colored blue, represent anticorrelated motions (C_{ij} = −1).

between the backbone and the complex was <3 Å. RMSF, R_g, and SASA also showed steady complex formation.

The g_mmpbsa tool computed the binding affinity of the protein−ligand complex using the MM-PBSA method. The free energy (kJ/mol) contribution of lead hits and standard molecules in relation to their respective targets is summarized in Table 4. In addition, detailed description of the total number of H-bond interactions in the protein−ligand complex has been shown in Supporting Information Figure S6A. Similarly, the contribution energy plot illustrated in Supporting Information Figure S6B exhibits the importance of the binding pocket residues in stable complex formation.

https://doi.org/10.1021/acsomega.3c00441
ACS Omega 2023, 8, 10565−10590

3.10. PCA and DCCM Analysis of Complexes. We employ PCA analysis to explore the dynamics of protein−ligand conformation for five complexes (two complexes with the reference drug and three complexes with the natural compound ligand) obtained from an MD simulation run of 50 ns. A PCA produces a matrix of eigenvectors and a list of related eigenvalues, which together represent the principal components and amplitudes of the internal movements of a protein. The first two eigenvectors/principal components (eigenvector 1 and eigenvector 2) are used to calculate the concerted motions of the past 50 ns trajectory since they can best describe the majority of the internal movements within a protein. The first two eigenvectors' 2D projection as well as the scatterplot are shown in Figure 7A. Captopril and Solasodine, two of the reference drugs employed in this study and directed at the MMP9 protein, were seen to have a greater range of conformations during the simulations (shown as a red and aqua line, respectively, in Figure 7A. Moreover, during simulation, the shortlisted MMP9-targeting ligands 7,4′-dihydroxyflavan, (3*R*)-3-(4-hydroxybenzyl)-6-hydroxy-8-methoxy-3,4-dihydro-2*H*-1-benzopyran, and MMP9-4′-hydroxy-7-methoxyflavan displayed less diversity than the reference drug (shown in blue, black, and green lines, respectively). Both the reference drugs demonstrated increased conformational flexibility with the maximum number of diverse conformations. Intriguingly, the MMP9 inhibitors 7,4′-dihydroxyflavan, (3*R*)-3-(4-hydroxybenzyl)-6-hydroxy-8-methoxy-3,4-dihydro-2*H*-1-benzopyran, and 4′-hydroxy-7-methoxyflavan took up substantially less conformational space than the Captopril reference drug. In contrast, only 7,4′-dihydroxyflavan, (3*R*)-3-(4-hydroxybenzyl)-6-hydroxy-8-methoxy-3,4-dihydro-2*H*-1-benzopyran performed better compared to the Solasodine reference drug as shown in the scatterplot (less dispersed plot). Therefore, we suggest that three lead-hit natural compounds could be more effective than the reference drugs.

The DCCM of Cα atoms in complexes provides a deeper structural understanding of the collective motion of the ligand-binding regions. The coordinated residual motion of the Cα atoms in each of the simulated complexes is shown in Figure 7B. Each residue exhibits a significant self-correlation with itself, as evidenced by the diagonal amber line. Scaling from amber to blue, respectively, is the strength of correlation (C_{ij} = 1) and anticorrelation (C_{ij} = −1). In complex MMP9-7,4′-dihydroxyflavan, the binding site residues show a positive correlation with the N-terminal domain of the MMP9. The scale of this correlation's amplitude goes from blue to amber color in smaller steps. Similarly, MMP9-MMP9-4′-hydroxy-7-methoxyflavan also showed a positive correlation with higher amplitude near binding site residues 222−249. In contrast, complex MMP9-44479222 showed anticorrelation, and its amplitude scaled from amber to blue color. The relevance of the active site residues in stabilizing the complexes was demonstrated by the coordinated motion displayed by the binding pocket residues spanning from 220 to 249 with the N-terminal region. The N-terminal residues of the MMP9 protein revealed a high association with the binding site residues of the reference ligands, such as Captopril and Solasodine. Comparing Captopril to the Solasodine ligand, the correlation magnitude was larger. The results showed that MMP9-containing natural compounds complexes and the reference ligand exhibited similar correlations near binding residues. In light of this, the DCCM displayed cooperative and anticooperative motion in the protein, indicating the conformational flexibility of the investigated complexes and stable connections mediated by noncooperative motion on the opposite side, which triggered the opening and shutting of the binding pocket residues and enabled the stable complex formation during the MD simulation.

4. DISCUSSION

The present study analyzed hypoxia, a critical microenvironmental condition of GBM, to identify potential biomarkers and establish treatment strategies for GBM treatment. In recent years, TME gained the attention of researchers as it regulates tumor growth and significantly influences treatment response. Hypoxia condition and immune cell infiltration in TME promote and antagonize tumor growth. Herein, we identify hypoxia-related molecular signatures involved in GBM pathogenesis. Based on the functional enrichment analysis, we have found 32 HUB signatures whose expressions were validated through microarray and RNA sequence data sets obtained from TCGA data sets of GBM patients. Indeed, we subjected 10 shortlisted molecular signatures to the RNA deconvolution-based TIMER analysis. From the gene expression profiles, TIMER employs an algorithm to determine the abundance of tumor-infiltrating immune cells. The proportion of cancer cells in the tumor tissue is described as tumor purity (also known as tumor cell fraction), which indicates the characteristics of TME. Recent studies have shown that tumor purity is linked to prognosis, mutation burden, and a robust immunological phenotype.[87,88] Our results indicate that LYN, MMP9, PSMB9, and TIMP1 were linked with the GBM microenvironment. Zhao et al. demonstrated a high expression of the PLOD family with negative tumor purity and high immune infiltration.[89] In our study, LYN was downregulated in the hypoxic condition in GBM. According to a study by Dai and Siemann, hypoxia has little to no impact on the expression of phosphorylated LYN.[90] However, the elevated MMP9 expression in hypoxic TME enhances DC infiltration and reduces the infiltration of cytotoxic T cells (CD8+ T cells).[91] In contrast, increased CD8+ T-cell infiltration had been linked to a better predictive factor for long-term survival in glioblastoma patients.[92] Additionally, PSMB8 and PSMB9 immunoproteasome subunits are overexpressed in melanoma cell lines, and their reduced expression is linked to a poor prognosis in nonsmall-cell lung carcinoma.[93] Herein, in this study, the reduced PSMB9 expression is linked to increased immune cell infiltration, with the exception of CD8+ T cells. Our findings are backed up by the fact that all members of the TIMP family had significantly higher levels of expression in GBM.[94] TIMP1 expression levels in hypoxic-GBM are exclusively correlated with DC infiltration and are inversely related to B cells and neutrophils. Consistent with our results, previous studies have also identified the four molecular signatures (LYN, TIMP1, MMP9, and PSMB9) as potential biomarkers associated with TME in GBM and other cancers.[95−97] Herein, we briefly discussed the relevant pathways mentioned above by starting with the ILK pathway known to promote cell growth, cell cycle progression, and increase VEGF expression by stimulating HIF-1 via a phosphatidylinositol 3-kinase (PI3K)−dependent activation.[98] Another significant pathway that is involved in the TME of GBM is the AP-1 transcription factor (dimeric in nature), which is made up of proteins from the Jun (c-Jun, JunB, and JunD) and Fos (c-Fos, FosB, Fra1, and Fra2) families. Studies have concluded that different triggers, such as inflammatory cytokines, stress inducers, or pathogens, activate the AP-1 transcription factor family, resulting in innate and

https://doi.org/10.1021/acsomega.3c00441
ACS Omega 2023, 8, 10565−10590

adaptive immunities.[99] In addition, active CDC42 (ρ-GTPase) has been shown to facilitate glioma cell migration and invasion and regulate cell polarity.[100] In GBM, HIF-1 and VEGF upregulate CXCR4, which is significant for angiogenesis and cell invasion.[101] Furthermore, another fascinating study showed that the interaction of microglia and GBM through the LPA pathway has important consequences for tumor progression. A deeper understanding of this interaction could lead to the development of new therapeutic techniques that target LPA as a possible GBM target.[102] Another study found that hypoxic TME stimulates invadopodia development (actin-rich protrusions of the plasma membrane that focus ECM breakdown through the secretion of MMPs), which are essential for metastasis.[103] In addition, our data showed that the localization of MMP9 was mainly the extracellular region, and FOS, JUN, and TP53 were only significantly overexpressed associated TFs in GBM patient's samples. MMP9 was overexpressed in different subtypes of GBM including classical, mesenchymal, neural, and proneural (shown in Supporting Information Figure S7A). It also has the potential to act as a poor prognostic biomarker (HR > 1) as it shows significant disease-free survival (shown in Supporting Information Figure S7B). This all together suggests the significance of targeting TME. LYN and PSMB9 being downregulated in hypoxic condition, and due to unavailability of the reported drug against TIMP1, these biomarkers were not explored in the current study in identifying the novel drug. Hence, MMP9 was selected for identifying natural compounds as inhibitors in order to reduce GBM pathogenesis.

MMP9, a member of the gelatinase family of MMPs that degrades and remodels ECM proteins, plays a vital role in cell migration and EMT and angiogenesis.[104] Other TME components, such as nonmalignant stromal cells, neutrophils, macrophages, and endothelial cells, release MMP9 in the microenvironment. MMPs are known to be induced by HIF-1.[105,106] MMP inhibitors can diminish tumor cells' invasive and migratory abilities in cancer. MMP9 inhibitors were previously discovered using a computational technique, indicating that MMP9 is a targetable protein.[107,108] Based on previous studies, we have selected Captopril and Solasodine as reference drugs against MMP9. Captopril is an MMP2 inhibitor for treating patients on continuous ambulatory peritoneal dialysis therapy.[109] Captopril inhibits MMP2 and MMP9 via chelating zinc ions at the enzyme's active site. It also utilized alongside other medicines like Disulfiram and Nelfinavir as adjuvant therapy for GBM.[110] Moreover, it can inhibit MMP2 and MMP9, suspected of having a role in GBM metastasis and invasion, since it is an angiotensin-converting enzyme inhibitor, which belongs to a family of metalloproteinases comparable to MMPs.[111] Similarly, Solasodine has been reported to inhibit MMP9 and induce cell apoptosis, particularly in human lung cancer. However, this drug's pharmacokinetics, safety, and effectiveness in clinical practice remain unclear.[85,112]

During identifying new agents for MMP9, we explored six classes of natural compounds, including alkaloids, flavonoids, terpenoids, aliphatic compounds, aromatic compounds, and tannins. Previous studies have also supported that multiple natural compounds have antitumor and apoptotic effects in TMZ and p53 resistance GBM cells. Various natural compounds such as chrysin, epigallocatechin-3-gallate, hispidulin, rutin, and silibinin were also used in combination with TMZ and other chemotherapeutic drugs due to their potential to act as chemosensitizers (such as icariin and quercetin), radiosensitizers (*Zataria multiflora*), inhibits proliferation (such as *Zingiber officinale* and *Rhazya stricta*) and migration, and induces apoptosis (Baicalein).[16,113,114] However, these were checked for BBB permeability, druglikeness, and LIPINSKI rules of 5, and ADMET analysis was performed. We performed in silico molecular docking and MD simulations with MMP9 protein (alpha chain) using Autodock Vina 4.0 and GROMACS to evaluate the inhibitory effect of shortlisted drugs. Ramachandran plot of MMP9 (PDB identifier: 4HMA) is shown in Supporting Information Figure S7C. The binding affinity of ligands (drugs) was calculated and compared with reference drugs. In this instance, we have picked three best-docked compounds with binding energies comparable to Solasodine and better than Captopril for MD simulations. Stability should be taken into careful consideration during drug testing in addition to safety. The software's MD simulation module examined the stability of these MMP9-compound complexes in the natural environment. Further compounds interacted with targets with a minimum of at least 2 H-bond interactions. Numerous studies have been conducted in the past to implement molecular docking and MD simulations and MM-PBSA assessment to record drug transport variability, identify protein allosteric inhibition, consider the impact of chirality in selective enzyme inhibition, investigate the irreversible style of the receptors, and evaluate ligand−protein interactions. Similarly, this study examined the intermolecular contact stability of identified prospective lead compounds and standard molecules with their respective targets using classical MD simulation for 50 ns of MMP9 protein with ligands.[115] Subsequently, the efficacy of molecules' molecular interactions can be examined using structural analysis, such as RMSD and RMSF.[116] Results revealed that the binding energy of MMP9 with ligands 7,4′-dihydroxyflavan, (3*R*)-3-(4-hydroxybenzyl)-6-hydroxy-8-methoxy-3,4-dihydro-2*H*-1-benzopyran, and 4′-hydroxy-7-methoxyflavan was similar (−10 kcal/mol) to that of the reference drug Solasodine and better than Captopril. All three ligands, flavonoids in nature, interact within the binding domain of the MMP9 pocket, and this interaction was stable for 50 ns with less deviation and fluctuations. RMSD value difference between the backbone and complex was <3 Å. The MMP9-7,4′-dihydroxyflavan complex findings suggest that five residues, Leu222, Val223, Ala242, Met247, and Tyr248, contributed significantly to the formation of the stable complex. Most importantly, the residues Tyr248 showed significant contributions to the binding affinity by scoring the lowest contribution energy of −5.41 kJ/mol. MMP9-(3*R*)-3-(4-hydroxybenzyl)-6-hydroxy-8-methoxy-3,4-dihydro-2*H*-1-benzopyran had a 94.16 kJ/mol determining binding affinity. Leu188, Leu222, Val223, His226, and Tyr248 residues also facilitated stable compound formation. Leu222 scored the highest binding affinity of −5.74 kJ/mol. Similarly, the binding energy of MMP9-4′-hydroxy-7-methoxyflavan was around 78.44 kJ/mol. The per-residue contribution energy also revealed that the formation of a stable complex was significantly influenced by six residues from the binding pocket: Leu188, Leu222, Val223, Leu243, Met247, and Tyr248. The binding affinity of the residue Met247 is −6.22 kJ/mol. Further, PCA analysis revealed that the MMP9-targeting ligands, 4′-dihydroxyflavan, (3*R*)-3-(4-hydroxybenzyl)-6-hydroxy-8-methoxy-3,4-dihydro-2*H*-1-benzopyran, and 4′-hydroxy-7-methoxyflavan had less diversity than the reference drug during the simulation run. Both reference drugs demonstrated increased conformational flexibility with the maximum number of diverse conformations. Interestingly, compared to the Captopril reference drug, the MMP9 inhibitors, 7,4′-dihydroxy-

https://doi.org/10.1021/acsomega.3c00441
ACS Omega 2023, 8, 10565−10590

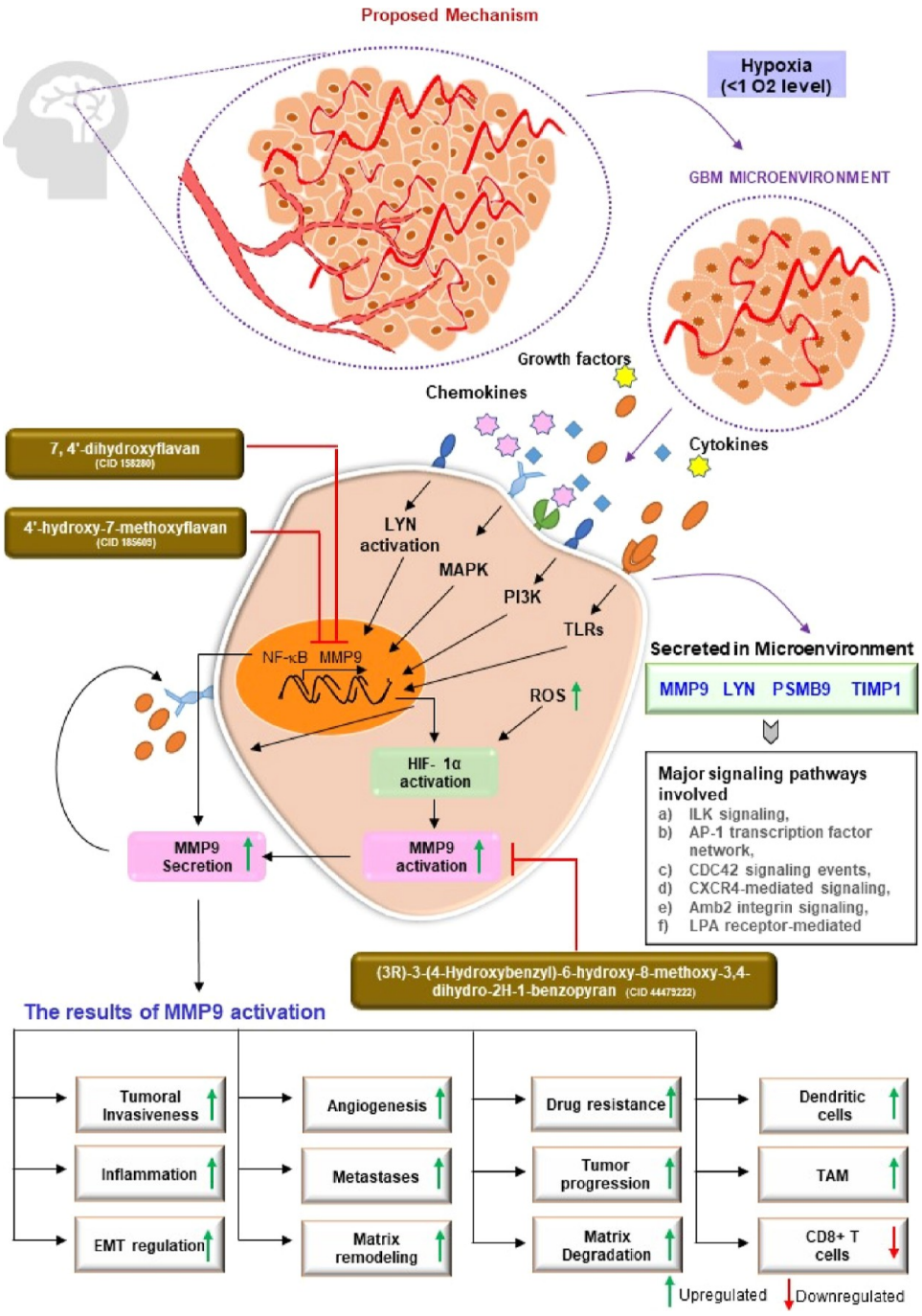

Figure 8. Potential of novel inhibitors 7,4′-dihydroxyflavan, (3*R*)-3-(4-hydroxybenzyl)-6-hydroxy-8-methoxy-3,4-dihydro-2*H*-1-benzopyran, and 4′-hydroxy-7-methoxyflavan in suppressing GBM pathogenesis by interacting with MMP9 protein produced in a hypoxic environment condition. MMP9 is synthesized de novo during stimulation induced with cytokines by activating various signaling pathways such as NF-κB, HIF-1, MAPK, PI3K, etc. Cytokines (TNF-α, IL-8, and IL-1β) and growth factors (TGF-β, PDGF, and bFGF) bind to their receptors which regulate MMP9 activation and secretion. MMP9 is secreted by tumor cells, monocytes, inflammatory macrophages, and stromal cells in the extracellular environment. This affects various downstream biological processes, including matrix degradation, remodeling, EMT (enhanced tumoral invasion, metastases), angiogenesis, inflammation, drug resistance, etc. Novel inhibitors 7,4′-dihydroxyflavan, (3*R*)-3-(4-hydroxybenzyl)-6-hydroxy-8-methoxy-3,4-dihydro-2*H*-1-benzopyran, and 4′-hydroxy-7-methoxyflavan bind to MMP9 and suppress its activation and thus reduce the expression and regulation of downstream process involved in GBM pathogenesis in the above figure. Our approaches to GBM treatment are being reoriented by focusing on these features of MMPs.

flavan, (3*R*)-3-(4-hydroxybenzyl)-6-hydroxy-8-methoxy-3,4-dihydro-2*H*-1-benzopyran, and 4′-hydroxy-7-methoxyflavan, used significantly less conformational space. Contrarily, only 7,4′-dihydroxyflavan and (3*R*)-3-(4-hydroxybenzyl)-6-hydroxy-8-methoxy-3,4-dihydro-2*H*-1-benzopyran outperformed the Solasodine reference drug.

Furthermore, 7,4′-dihydroxyflavan, (3*R*)-3-(4-hydroxybenzyl)-6-hydroxy-8-methoxy-3,4-dihydro-2*H*-1-benzopyran, and 4′-hydroxy-7-methoxyflavan showed positive correlations with

https://doi.org/10.1021/acsomega.3c00441
ACS Omega 2023, 8, 10565−10590

the N-terminal domain of proteins, while (3*R*)-3-(4-hydroxybenzyl)-6-hydroxy-8-methoxy-3,4-dihydro-2*H*-1-benzopyran displayed an anticorrelation. As a result, we demonstrated how three lead flavonoids may be able to target the MMP9 protein. The fact that 7,4′-dihydroxyflavan was derived from the African forest tree *Guibourtia ehie* or Shedua, which has been utilized traditionally for tumor and wound healing, provided additional support for our findings in earlier investigations. It acts as a metabolite and shows anti-inflammatory and antioxidant effects in prostate cancer, breast cancer, and osteosarcoma by regulating Akt/Bad and MAPK signaling. In addition, (3*R*)-3-(4-hydroxybenzyl)-6-hydroxy-8-methoxy-3,4-dihydro-2*H*-1-benzopyran was found in *Soymida febrifuge* (Indian-redwood). Its fruits are therapeutic and have been used to treat cervical and colon cancer.[117] Interestingly, a study by Sowmyya and Vijaya Lakshmi discovered that extracts from these dried fruits contributed to the creation of silver nanoparticles by acting as reducing and stabilizing agents during the conversion of Ag^+ to nano-silver.[118] The last compound, 4′-hydroxy-7-methoxyflavan, was derived from the orchid tree *Bauhinia divaricate* and was formerly used to treat skin and colon cancer. These three flavonoids will inhibit MMP9 and lower its overexpression brought on by hypoxia in GBM. As a result of these inhibitions, the downstream effects of MMP9 activation will be diminished, which will minimize the pathogenesis of GBM. Cell proliferation, invasion, angiogenesis, drug resistance, matrix remodeling, and immune cell infiltration are significant pathways that will be impacted. The infiltration of DCs in response to MMP9 overexpression was also demonstrated by our data, which also indicated a positive correlation with immune checkpoints like PD-1 and TIM-3. Figure 8 illustrates the proposed mode of action for three novel flavonoids, including 7,4′-dihydroxyflavan (PubChem CID 158280), (3*R*)-3-(4-hydroxybenzyl)-6-hydroxy-8-methoxy-3,4-dihydro-2*H*-1-benzopyran (PubChem CID 44479222), and 4′-hydroxy-7-methoxyflavan (PubChem CID 185609). These will attenuate MMP9 activation's impact on GBM.

5. CONCLUSIONS AND FUTURE PERSPECTIVES

Despite recent advancements in chemotherapy, radiotherapy, and immunotherapy, there is currently no satisfactory therapy for GBM in clinics due to many reasons, being toxicity of chemotherapy, failure of the drug to cross BBB, involvement of TME, and less immune infiltration. For instance, immune checkpoint blockade targeting CD8+ T cells is ineffective for GBM.[119] There is an unmet need for novel approaches to treat GBM and other brain cancers. Here in our study, we have focused on a crucial TME parameter, that is, hypoxia caused due to intense cell respiration, excessive nutrient consumption by tumor cells, and abnormal vasculature. However, hypoxia is a hallmark of brain tumors, and if and how hypoxia affects antitumor immunity in the brain remains unclear. Our findings shed light on the potential of MMP9 as a therapeutic target and a robust biomarker in GBM's hypoxic microenvironment. In Figure 8, it is illustrated that in response to cytokine-induced stimulation, MMP9 is synthesized de novo by activating various signaling pathways including NF-κB, HIF-1, MAPK, PI3K, and so forth. Cytokines such as TNF-α, IL-8, and IL-1β and growth factors namely TGF-β, PDGF, and bFGF bind to their respective receptors and influence the activation and production of MMP9. This has an impact on a number of biological functions that come thereafter, such as drug resistance, remodeling of the matrix, EMT, increased tumoral invasion, metastases, angiogenesis, and remodeling.

Previous studies supported our results where researchers have shown that MMP9, a zinc-dependent endopeptidase, was upregulated in glioma tissues, and its expression was correlated with tumor grade and poor prognosis. Hypoxia condition increases the protein expression of HIF-α, MMP2, and MMP9 in cancer[120] and regulates tight junction rearrangement, leading to vascular leakage in the brain.[121] Majority of the ECM components are substrates of MMPs. MMP-9 can cleave many ECM proteins to regulate ECM remodeling and affects the alteration of cell−cell and cell−ECM interactions. It can also cleave many plasma surface proteins to release them from the cell surface. It has been implicated in the invasion and also implicated in BBB opening as part of the neuroinflammatory response, metastasis through proliferation, vasculogenesis, and angiogenesis.[72] MMP9 has been a potential biomarker for many cancers, including osteosarcoma, breast, cervical, ovarian, and pancreatic, giant cell tumor of bone, and non-small cell lung cancer.[21] Herein the current study, we have proposed MMP9 as a promising biomarker for hypoxic microenvironmental conditions in GBM. Other molecular signatures, such as LYN, PSMB9, and TIMP1, could be investigated further as druggable biomarkers or prognostic markers in addition to MMP9. Infiltration of immune cells such as neutrophils and DCs was linked to this gene's expression to varying degrees. This effect opens up new avenues for study into MMP9 and GBM. A negative correlation with B cells, CD4+ T cells, and CD8+ T cells supports the failure of current immune checkpoint inhibitors.

The current study used in silico techniques such as compound-protein-pathway enrichment analysis, network pharmacology, molecular docking, MD simulation, MM-PBSA, PCA, and DCCM investigations to identify a collection of druggable and nontoxic natural compounds from plants. The potential of natural compounds to be used as drugs was revealed by ADMET analysis of 11 novel hits. A chemical substance must have absorption, distribution, metabolism, excretion, and toxicity values to be utilized as a medication. The results obtained showed flavonoids named 7,4′-dihydroxyflavan, (3*R*)-3-(4-hydroxybenzyl)-6-hydroxy-8-methoxy-3,4-dihydro-2*H*-1-benzopyran, and 4′-hydroxy-7-methoxyflavan as potential inhibitors of MMP9 produced from the hypoxic condition in GBM. These inhibitors have comparable or better results compared to reference drugs Solasodine and Captopril. Our results indicate that MMP9 and drug interaction are stable, and proposed novel flavonoids can inhibit or reduce MMP9 expression in hypoxia conditions, which will further affect the downstream process involved in GBM pathogenesis. Hence, targeting an essential microenvironmental condition will improve therapeutic efficacy and expand the treatment drug library against GBM. Limiting to the present findings, we point out that the results presented in this work are based on processor simulations which need to be further validated with wet-lab experimental protocols.

In conclusion, the observations of this work suggest novel plant-based flavonoids inhibited the potential role of MMP9 as a biomarker factor and active MMP9 in GBM. Prior to synthesizing therapeutics, the results of this investigation could be helpful. Other natural compounds and plant-based natural compounds could be examined and studied to understand and explore whether they could be employed as future possibilities for GBM medicines. The results of this study

https://doi.org/10.1021/acsomega.3c00441
ACS Omega 2023, 8, 10565−10590

are helpful for drug development. The findings may aid in the assisted screening of therapeutics for GBM. This study is novel in incorporating various computational methodologies for the virtual screening of natural compounds based on BBB, ADMET, PAINS, and Lipinski's rule. This study allows scientists to explore these molecules in vitro or in vivo as a medicinal approach. We have validated our results using different computational methodologies such as multiple-target validation, literature validation, TCGA databases (containing GBM samples data), cell culture, and animal model research which will fill in the gaps. We identified the common residues via which the inhibitor can potentially bind to the target using bioinformatics tools and in silico studies. However, the molecular mechanism underlying the reduction of target expression needs only to be validated through in vitro experiments. New leads are being discovered in several ongoing studies using advanced computational strategies and machine learning models to filter massive pharmaceutical libraries. The experimental screening strategy alone may not enhance lead productivity for the rapid development of viable medicines. Our findings will aid researchers in concentrating on TME components and their conditions in order to produce novel natural product-based anti-GBM therapies that address two major issues: toxicity and resistance and target of a major microenvironmental condition hypoxia.

■ ASSOCIATED CONTENT

Supporting Information

The Supporting Information is available free of charge at https://pubs.acs.org/doi/10.1021/acsomega.3c00441.

MA plot; list of DEGs; mutational and correlation analyses; localization and transcription factor analysis; screening of natural compounds; physiochemical properties; 2D docked structure; H-bond and contribution energy plot; and MMP9 characteristics (PDF)

■ AUTHOR INFORMATION

Corresponding Author

Pravir Kumar − *Molecular Neuroscience and Functional Genomics Laboratory, Department of Biotechnology, Delhi Technological University (Formerly DCE), Delhi 110042, India;* orcid.org/0000-0001-7444-2344; Phone: +91-9818898622; Email: pravirkumar@dtu.ac.in

Author

Smita Kumari − *Molecular Neuroscience and Functional Genomics Laboratory, Department of Biotechnology, Delhi Technological University (Formerly DCE), Delhi 110042, India*

Complete contact information is available at: https://pubs.acs.org/10.1021/acsomega.3c00441

Author Contributions

P.K. and S.K. conceived and designed the manuscript. S.K. collected, analyzed, and critically evaluated these data. S.K. prepared the figures and tables. P.K. and S.K. analyzed the entire data and wrote the manuscript.

Funding

S.K. has received Senior Research Fellowship (SRF) from the Department of Biotechnology (DBT), Govt. of India (Fellow ID: DBT/2019/DTU/1308).

Notes

The authors declare no competing financial interest.

■ ACKNOWLEDGMENTS

We would like to thank the senior management of Delhi Technological University (DTU) and the Department of Biotechnology (DBT), Government of India, for their constant support and financial assistance.

■ LIST OF ABBREVIATIONS

2D, 2-dimensional; 3D, 3-dimensional; Caco-2, colon adenocarcinoma cell lines; DCCM, domain cross-correlation matrix; DEGs, differentially regulated genes; DCs, dendritic cells; EPO, erythropoietin; GBM, glioblastoma multiforme; GEO, gene expression omnibus; GEPIA2.0, Gene Expression Profiling Interactive Analysis; GMQE, Global Model Quality Estimate; GS2D, gene set to diseases; HBA, hydrogen bond acceptor; HBD, hydrogen bond donor; H-bond, hydrogen bond; HIA, human intestinal absorption cells; HR, hazard ratio; KEGG, Kyoto Encyclopedia of Genes and Genomes; logCPM, log_2-counts-per-millions; LYN, Lck/Yes-related novel protein tyrosine kinase; MB-PBSA, molecular mechanics Poisson−Boltzmann surface area; MD, molecular dynamics; MDCK, Madin−Darby canine kidney cells; MMP-9, matrix metalloproteinase 9; MW, molecular weight; PAINS, Pan Assay Interference Compounds; PCA, principal component analysis; PDGF, platelet-derived growth factor; PPI, protein−protein interaction; PSMB9, proteasome 20S subunit beta 9; RCSB, Research Collaboratory for Structural Bioinformatics; RMSD, root-mean-square deviation; RMSF, root-mean-square fluctuation; R_g, radiation of gyration; SASA, solvent accessible surface area; SMILES, Simplified Molecular-Input Line-Entry System; STRING, Search Tool for the Retrieval of Interacting Genes/Proteins; TFs, transcription factors; TIMP1, tissue inhibitor of metalloproteinases 1; TME, tumor microenvironment; TPM, transcript per million; vdw, van der Waal force; VEGF, vascular endothelial growth factor

■ REFERENCES

(1) Miller, K. D.; Ostrom, Q. T.; Kruchko, C.; Patil, N.; Tihan, T.; Cioffi, G.; Fuchs, H. E.; Waite, K. A.; Jemal, A.; Siegel, R. L.; Barnholtz-Sloan, J. S. Brain and Other Central Nervous System Tumor Statistics, 2021. *Ca -Cancer J. Clin.* **2021**, *71*, 381−406.

(2) Stylli, S. S. Novel Treatment Strategies for Glioblastoma. *Cancers* **2020**, *12*, 2883.

(3) DeCordova, S.; Shastri, A.; Tsolaki, A. G.; Yasmin, H.; Klein, L.; Singh, S. K.; Kishore, U. Molecular Heterogeneity and Immunosuppressive Microenvironment in Glioblastoma. *Front. Immunol.* **2020**, *11*, 1402.

(4) Li, Y.; Zhao, L.; Li, X. F. Hypoxia and the Tumor Microenvironment. *Technol. Cancer Res. Treat.* **2021**, *20*, 153303382110363.

(5) Huang, W. J.; Chen, W. W.; Zhang, X. Glioblastoma Multiforme: Effect of Hypoxia and Hypoxia Inducible Factors on Therapeutic Approaches (Review). *Oncol. Lett.* **2016**, *12*, 2283−2288.

(6) Velásquez, C.; Mansouri, S.; Gutiérrez, O.; Mamatjan, Y.; Mollinedo, P.; Karimi, S.; Singh, O.; Terán, N.; Martino, J.; Zadeh, G.; Fernández-Luna, J. L. Hypoxia Can Induce Migration of Glioblastoma Cells through a Methylation-Dependent Control of ODZ1 Gene Expression. *Front. Oncol.* **2019**, *9*, 1036.

(7) Emami Nejad, A.; Najafgholian, S.; Rostami, A.; Sistani, A.; Shojaeifar, S.; Esparvarinha, M.; Nedaeinia, R.; Haghjooy Javanmard, S.; Taherian, M.; Ahmadlou, M.; Salehi, R.; Sadeghi, B.; Manian, M. The Role of Hypoxia in the Tumor Microenvironment and Development of Cancer Stem Cell: A Novel Approach to Developing Treatment. *Cancer Cell Int.* **2021**, *21*, 62.

(8) Zheng, X.; Qian, Y.; Fu, B.; Jiao, D.; Jiang, Y.; Chen, P.; Shen, Y.; Zhang, H.; Sun, R.; Tian, Z.; Wei, H. Mitochondrial Fragmentation Limits NK Cell-Based Tumor Immunosurveillance. *Nat. Immunol.* **2019**, *20*, 1656−1667.
(9) Henze, A. T.; Mazzone, M. The Impact of Hypoxia on Tumor-Associated Macrophages. *J. Clin. Invest.* **2016**, *126*, 3672.
(10) Park, J. H.; Kim, H. J.; Kim, C. W.; Kim, H. C.; Jung, Y.; Lee, H. S.; Lee, Y.; Ju, Y. S.; Oh, J. E.; Park, S. H.; Lee, J. H.; Lee, S. K.; Lee, H. K. Tumor Hypoxia Represses Γδ T Cell-Mediated Antitumor Immunity against Brain Tumors. *Nat. Immunol.* **2021**, *22*, 336−346.
(11) Bronisz, A.; Salińska, E.; Chiocca, E. A.; Godlewski, J. Hypoxic Roadmap of Glioblastoma-Learning about Directions and Distances in the Brain Tumor Environment. *Cancers* **2020**, *12*, 1213.
(12) Kalkan, R. Hypoxia Is the Driving Force Behind GBM and Could Be a New Tool in GBM Treatment. *Crit. Rev. Eukaryot. Gene Expr.* **2015**, *25*, 363−369.
(13) Tan, A. C.; Ashley, D. M.; López, G. Y.; Malinzak, M.; Friedman, H. S.; Khasraw, M. Management of Glioblastoma: State of the Art and Future Directions. *Ca -Cancer J. Clin.* **2020**, *70*, 299−312.
(14) Atanasov, A. G.; Zotchev, S. B.; Dirsch, V. M.; Orhan, I. E.; Supuran, M.; Rollinger, J. M.; Barreca, D.; Weckwerth, W.; Bauer, R.; Bayer, E. A.; Majeed, M.; Bishayee, A.; Bochkov, V.; Bonn, G. K.; Braidy, N.; Bucar, F.; Cifuentes, A.; D'Onofrio, G.; Bodkin, M.; Diederich, M.; Dinkova-Kostova, A. T.; Efferth, T.; El Bairi, K.; Arkells, N.; Fan, T. P.; Fiebich, B. L.; Freissmuth, M.; Georgiev, M. I.; Gibbons, S.; Godfrey, K. M.; Gruber, C. W.; Heer, J.; Huber, L. A.; Ibanez, E.; Kijjoa, A.; Kiss, A. K.; Lu, A.; Macias, F. A.; Miller, M. J. S.; Mocan, A.; Müller, R.; Nicoletti, F.; Perry, G.; Pittalà, V.; Rastrelli, L.; Ristow, M.; Russo, G. L.; Silva, A. S.; Schuster, D.; Sheridan, H.; Skalicka-Woźniak, K.; Skaltsounis, L.; Sobarzo-Sánchez, E.; Bredt, D. S.; Stuppner, H.; Sureda, A.; Tzvetkov, N. T.; Vacca, R. A.; Aggarwal, B. B.; Battino, M.; Giampieri, F.; Wink, M.; Wolfender, J. L.; Xiao, J.; Yeung, A. W. K.; Lizard, G.; Popp, M. A.; Heinrich, M.; Berindan-Neagoe, I.; Stadler, M.; Daglia, M.; Verpoorte, R.; Supuran, C. T. Natural Products in Drug Discovery: Advances and Opportunities. *Nat. Rev. Drug Discovery* **2021**, *20*, 200−216.
(15) Huang, M.; Lu, J. J.; Ding, J. Natural Products in Cancer Therapy: Past, Present and Future. *Nat. Prod. Bioprospect.* **2021**, *11*, 5−13.
(16) Vengoji, R.; Macha, M. A.; Batra, S. K.; Shonka, N. A. Natural Products: A Hope for Glioblastoma Patients. *Oncotarget* **2018**, *9*, 22194.
(17) Santos, B. L.; Oliveira, M. N.; Coelho, P. L. C.; Pitanga, B. P. S.; da Silva, A. B.; Adelita, T.; Silva, V. D. A.; Costa, M. D. F. D.; El-Bachá, R. S.; Tardy, M.; Chneiweiss, H.; Junier, M. P.; Moura-Neto, V.; Costa, S. L. Flavonoids Suppress Human Glioblastoma Cell Growth by Inhibiting Cell Metabolism, Migration, and by Regulating Extracellular Matrix Proteins and Metalloproteinases Expression. *Chem. Biol. Interact.* **2015**, *242*, 123−138.
(18) Soukhtanloo, M.; Mohtashami, E.; Maghrouni, A.; Mollazadeh, H.; Mousavi, S. H.; Roshan, M. K.; Tabatabaeizadeh, S. A.; Hosseini, A.; Vahedi, M. M.; Jalili-Nik, M.; Afshari, A. R. Natural Products as Promising Targets in Glioblastoma Multiforme: A Focus on NF-KB Signaling Pathway. *Pharmacol. Rep.* **2020**, *72*, 285−295.
(19) Zhai, K.; Siddiqui, M.; Abdellatif, B.; Liskova, A.; Kubatka, P.; Büsselberg, D. Natural Compounds in Glioblastoma Therapy: Preclinical Insights, Mechanistic Pathways, and Outlook. *Cancers* **2021**, *13*, 2317.
(20) Pujada, A.; Walter, L.; Patel, A.; Bui, T. A.; Zhang, Z.; Zhang, Y.; Denning, T. L.; Garg, P. Matrix Metalloproteinase MMP9 Maintains Epithelial Barrier Function and Preserves Mucosal Lining in Colitis Associated Cancer. *Oncotarget* **2017**, *8*, 94650.
(21) Huang, H. Matrix Metalloproteinase-9 (MMP-9) as a Cancer Biomarker and MMP-9 Biosensors: Recent Advances. *Sensors* **2018**, *18*, 3249.
(22) Augoff, K.; Hryniewicz-Jankowska, A.; Tabola, R.; Stach, K. MMP9: A Tough Target for Targeted Therapy for Cancer. *Cancers* **2022**, *14*, 1847.
(23) Atiq, A.; Parhar, I. Anti-Neoplastic Potential of Flavonoids and Polysaccharide Phytochemicals in Glioblastoma. *Molecules* **2020**, *25*, 4895.
(24) Mondal, A.; Gandhi, A.; Fimognari, C.; Atanasov, A. G.; Bishayee, A. Alkaloids for Cancer Prevention and Therapy: Current Progress and Future Perspectives. *Eur. J. Pharmacol.* **2019**, *858*, 172472.
(25) Edgar, R.; Domrachev, M.; Lash, A. E. Gene Expression Omnibus: NCBI Gene Expression and Hybridization Array Data Repository. *Nucleic Acids Res.* **2002**, *30*, 207−210.
(26) Mahi, N. A.; Najafabadi, M. F.; Pilarczyk, M.; Kouril, M.; Medvedovic, M. GREIN: An Interactive Web Platform for Re-Analyzing GEO RNA-Seq Data. *Sci. Rep.* **2019**, *9*, 7580.
(27) Huang, D. W.; Sherman, B. T.; Lempicki, R. A. Bioinformatics Enrichment Tools: Paths toward the Comprehensive Functional Analysis of Large Gene Lists. *Nucleic Acids Res.* **2009**, *37*, 1−13.
(28) Fontaine, J. F.; Andrade-Navarro, M. A. Gene Set to Diseases (GS2D): Disease Enrichment Analysis on Human Gene Sets with Literature Data. *Genomics Comput. Biol.* **2016**, *2*, No. e33.
(29) Kuleshov, M. V.; Jones, M. R.; Rouillard, A. D.; Fernandez, N. F.; Duan, Q.; Wang, Z.; Koplev, S.; Jenkins, S. L.; Jagodnik, K. M.; Lachmann, A.; McDermott, M. G.; Monteiro, C. D.; Gundersen, G. W.; Ma'ayan, A. Enrichr: a comprehensive gene set enrichment analysis web server 2016 update. *Nucleic Acids Res.* **2016**, *44*, W90−W97.
(30) Chen, E. Y.; Tan, C. M.; Kou, Y.; Duan, Q.; Wang, Z.; Meirelles, G. V.; Clark, N. R.; Ma'ayan, A. Enrichr: Interactive and Collaborative HTML5 Gene List Enrichment Analysis Tool. *BMC Bioinf.* **2013**, *14*, 128.
(31) Pathan, M.; Keerthikumar, S.; Ang, C. S.; Gangoda, L.; Quek, C. Y. J.; Williamson, N. A.; Mouradov, D.; Sieber, O. M.; Simpson, R. J.; Salim, A.; Bacic, A.; Hill, A. F.; Stroud, D. A.; Ryan, M. T.; Agbinya, J. I.; Mariadason, J. M.; Burgess, A. W.; Mathivanan, S. FunRich: An Open Access Standalone Functional Enrichment and Interaction Network Analysis Tool. *Proteomics* **2015**, *15*, 2597−2601.
(32) Szklarczyk, D.; Gable, A. L.; Nastou, K. C.; Lyon, D.; Kirsch, R.; Pyysalo, S.; Doncheva, N. T.; Legeay, M.; Fang, T.; Bork, P.; Jensen, L. J.; von Mering, C. The STRING Database in 2021: Customizable Protein-Protein Networks, and Functional Characterization of User-Uploaded Gene/Measurement Sets. *Nucleic Acids Res.* **2021**, *49*, D605−D612.
(33) Shannon, P.; Markiel, A.; Ozier, O.; Baliga, N. S.; Wang, J. T.; Ramage, D.; Amin, N.; Schwikowski, B.; Ideker, T. Cytoscape: A Software Environment for Integrated Models of Biomolecular Interaction Networks. *Genome Res.* **2003**, *13*, 2498−2504.
(34) Li, T.; Fu, J.; Zeng, Z.; Cohen, D.; Li, J.; Chen, Q.; Li, B.; Liu, X. S. TIMER2.0 for Analysis of Tumor-Infiltrating Immune Cells. *Nucleic Acids Res.* **2020**, *48*, W509−W514.
(35) Bowman, R. L.; Wang, Q.; Carro, A.; Verhaak, R. G. W.; Squatrito, M. GlioVis Data Portal for Visualization and Analysis of Brain Tumor Expression Data sets. *Neuro Oncol.* **2017**, *19*, 139−141.
(36) Tang, Z.; Kang, B.; Li, C.; Chen, T.; Zhang, Z. GEPIA2: An Enhanced Web Server for Large-Scale Expression Profiling and Interactive Analysis. *Nucleic Acids Res.* **2019**, *47*, W556−W560.
(37) Gill, B. J.; Pisapia, D. J.; Malone, H. R.; Goldstein, H.; Lei, L.; Sonabend, A.; Yun, J.; Samanamud, J.; Sims, J. S.; Banu, M.; Dovas, A.; Teich, A. F.; Sheth, S. A.; McKhann, G. M.; Sisti, M. B.; Bruce, J. N.; Sims, P. A.; Canoll, P. MRI-Localized Biopsies Reveal Subtype-Specific Differences in Molecular and Cellular Composition at the Margins of Glioblastoma. *Proc. Natl. Acad. Sci. U.S.A.* **2014**, *111*, 12550−12555.
(38) Madhavan, S.; Zenklusen, J. C.; Kotliarov, Y.; Sahni, H.; Fine, H. A.; Buetow, K. Rembrandt: Helping Personalized Medicine Become a Reality through Integrative Translational Research. *Mol. Cancer Res.* **2009**, *7*, 157−167.
(39) Gravendeel, L. A. M.; Kouwenhoven, M. C. M.; Gevaert, O.; de Rooi, J. J.; Stubbs, A. P.; Duijm, J. E.; Daemen, A.; Bleeker, F. E.; Bralten, L. B. C.; Kloosterhof, N. K.; De Moor, B.; Eilers, P. H. C.; van der Spek, P. J.; Kros, J. M.; Sillevis Smitt, P. A. E.; van den Bent, M. J.; French, P. J. Intrinsic Gene Expression Profiles of Gliomas Are a Better Predictor of Survival than Histology. *Cancer Res.* **2009**, *69*, 9065−9072.

https://doi.org/10.1021/acsomega.3c00441
ACS Omega 2023, 8, 10565−10590

(40) Li, T.; Fan, J.; Wang, B.; Traugh, N.; Chen, Q.; Liu, J. S.; Li, B.; Liu, X. S. TIMER: A Web Server for Comprehensive Analysis of Tumor-Infiltrating Immune Cells. *Cancer Res.* **2017**, *77*, e108−e110.
(41) Yu, C. S.; Chen, Y. C.; Lu, C. H.; Hwang, J. K. Prediction of Protein Subcellular Localization. *Proteins: Struct., Funct., Bioinf.* **2006**, *64*, 643−651.
(42) Fornes, O.; Castro-Mondragon, J. A.; Khan, A.; van der Lee, R.; Zhang, X.; Richmond, P. A.; Modi, B. P.; Correard, S.; Gheorghe, M.; Baranašić, D.; Santana-Garcia, W.; Tan, G.; Chèneby, J.; Ballester, B.; Parcy, F.; Sandelin, A.; Lenhard, B.; Wasserman, W. W.; Mathelier, A. JASPAR 2020: Update of the Open-Access Database of Transcription Factor Binding Profiles. *Nucleic Acids Res.* **2020**, *48*, D87.
(43) Zhou, G.; Soufan, O.; Ewald, J.; Hancock, R. E. W.; Basu, N.; Xia, J. NetworkAnalyst 3.0: A Visual Analytics Platform for Comprehensive Gene Expression Profiling and Meta-Analysis. *Nucleic Acids Res.* **2019**, *47*, W234−W241.
(44) Mangal, M.; Sagar, P.; Singh, H.; Raghava, G. P. S.; Agarwal, S. M. NPACT: Naturally Occurring Plant-Based Anti-Cancer Compound-Activity-Target Database. *Nucleic Acids Res.* **2013**, *41*, D1124.
(45) Angeli, E.; Nguyen, T. T.; Janin, A.; Bousquet, G. How to Make Anticancer Drugs Cross the Blood-Brain Barrier to Treat Brain Metastases. *Int. J. Mol. Sci.* **2019**, *21*, 22.
(46) Daina, A.; Michielin, O.; Zoete, V. SwissADME: A Free Web Tool to Evaluate Pharmacokinetics, Drug-Likeness and Medicinal Chemistry Friendliness of Small Molecules. *Sci. Rep.* **2017**, *7*, 42717.
(47) Liu, H.; Wang, L.; Lv, M.; Pei, R.; Li, P.; Pei, Z.; Wang, Y.; Su, W.; Xie, X. Q. AlzPlatform: An Alzheimer's Disease Domain-Specific Chemogenomics Knowledgebase for Polypharmacology and Target Identification Research. *J. Chem. Inf. Model.* **2014**, *54*, 1050−1060.
(48) Molsoft L. L. C. Drug-Likeness and molecular property prediction. https://molsoft.com/mprop/ (accessed Dec 26, 2021).
(49) Xiong, G.; Wu, Z.; Yi, J.; Fu, L.; Yang, Z.; Hsieh, C.; Yin, M.; Zeng, X.; Wu, C.; Lu, A.; Chen, X.; Hou, T.; Cao, D. ADMETlab 2.0: An Integrated Online Platform for Accurate and Comprehensive Predictions of ADMET Properties. *Nucleic Acids Res.* **2021**, *49*, W5−W14.
(50) BIOVIA Discovery Studio Visualizer-Dassault Systèmes. https://discover.3ds.com/discovery-studio-visualizer-download (accessed Sep 11, 2022). Free Download.
(51) Rappe, A. K.; Casewit, C. J.; Colwell, K. S.; Goddard, W. A.; Skiff, W. M. UFF, a Full Periodic Table Force Field for Molecular Mechanics and Molecular Dynamics Simulations. *J. Am. Chem. Soc.* **1992**, *114*, 10024−10035.
(52) Anderson, R. J.; Weng, Z.; Campbell, R. K.; Jiang, X. Main-Chain Conformational Tendencies of Amino Acids. *Proteins* **2005**, *60*, 679−689.
(53) Colovos, C.; Yeates, T. O. Verification of Protein Structures: Patterns of Nonbonded Atomic Interactions. *Protein Sci.* **1993**, *2*, 1511−1519.
(54) Bowie, J. U.; Lüthy, R.; Eisenberg, D. A Method to Identify Protein Sequences That Fold into a Known Three-Dimensional Structure. *Science* **1991**, *253*, 164−170.
(55) Samdani, A.; Vetrivel, U. POAP: A GNU Parallel Based Multithreaded Pipeline of Open Babel and AutoDock Suite for Boosted High Throughput Virtual Screening. *Comput. Biol. Chem.* **2018**, *74*, 39−48.
(56) Van Der Spoel, D.; Lindahl, E.; Hess, B.; Groenhof, G.; Mark, A. E.; Berendsen, H. J. C. GROMACS: Fast, Flexible, and Free. *J. Comput. Chem.* **2005**, *26*, 1701−1718.
(57) Kumari, R.; Kumar, R.; Lynn, A. G_mmpbsa–a GROMACS Tool for High-Throughput MM-PBSA Calculations. *J. Chem. Inf. Model.* **2014**, *54*, 1951−1962.
(58) Bhandare, V. V.; Kumbhar, B. V.; Kunwar, A. Differential Binding Affinity of Tau Repeat Region R2 with Neuronal-Specific β-Tubulin Isotypes. *Sci. Rep.* **2019**, *9*, 10795.
(59) Dwivedi, P. S. R.; Patil, V. S.; Khanal, P.; Bhandare, V. V.; Gurav, S.; Harish, D. R.; Patil, B. M.; Roy, S. System Biology-Based Investigation of Silymarin to Trace Hepatoprotective Effect. *Comput. Biol. Med.* **2022**, *142*, 105223.
(60) Taidi, L.; Maurady, A.; Britel, M. R. Molecular Docking Study and Molecular Dynamic Simulation of Human Cyclooxygenase-2 (COX-2) with Selected Eutypoids. *J. Biomol. Struct. Dyn.* **2020**, *40*, 1189−1204.
(61) Khanal, P.; Patil, V. S.; Bhandare, V. V.; Dwivedi, P. S. R.; Shastry, C. S.; Patil, B. M.; Gurav, S. S.; Harish, D. R.; Roy, S. Computational Investigation of Benzalacetophenone Derivatives against SARS-CoV-2 as Potential Multi-Target Bioactive Compounds. *Comput. Biol. Med.* **2022**, *146*, 105668.
(62) Bhandare, V. V.; Ramaswamy, A. The Proteinopathy of D169G and K263E Mutants at the RNA Recognition Motif (RRM) Domain of Tar DNA-Binding Protein (Tdp43) Causing Neurological Disorders: A Computational Study. *J. Biomol. Struct. Dyn.* **2018**, *36*, 1075−1093.
(63) Arnold, G. E.; Ornstein, R. L. Molecular Dynamics Study of Time-Correlated Protein Domain Motions and Molecular Flexibility: Cytochrome P450BM-3. *Biophys. J.* **1997**, *73*, 1147−1159.
(64) Khanal, P.; Zargari, F.; Far, B. F.; Kumar, D.; R, M.; Mahdi, Y. K.; Jubair, N. K.; Saraf, S. K.; Bansal, P.; Singh, R.; Selvaraja, M.; Dey, Y. N. Integration of System Biology Tools to Investigate Huperzine A as an Anti-Alzheimer Agent. *Front. Pharmacol.* **2021**, *12*, 785964.
(65) Mahi, N. A.; Najafabadi, M. F.; Pilarczyk, M.; Kouril, M.; Medvedovic, M. GREIN: An Interactive Web Platform for Reanalyzing GEO RNA-Seq Data. *Sci. Rep.* **2019**, *9*, 7580.
(66) Venny 2.1.0. https://bioinfogp.cnb.csic.es/tools/venny/index.html (accessed Nov 29, 2021).
(67) Vassilakopoulou, M.; Won, M.; Curran, W. J.; Souhami, L.; Prados, M. D.; Langer, C. J.; Rimm, D. L.; Hanna, J. A.; Neumeister, V. M.; Melian, E.; Diaz, A. Z.; Atkins, J. N.; Komarnicky, L. T.; Schultz, C. J.; Howard, S. P.; Zhang, P.; Dicker, A. P.; Knisely, J. P. S. BRCA1 Protein Expression Predicts Survival in Glioblastoma Patients from an NRG Oncology RTOG Cohort. *Oncology* **2021**, *99*, 580.
(68) Zhang, Y.; Xia, Q.; Lin, J. Identification of the Potential Oncogenes in Glioblastoma Based on Bioinformatic Analysis and Elucidation of the Underlying Mechanisms. *Oncol. Rep.* **2018**, *40*, 715−725.
(69) Yang, G.; Dong, K.; Zhang, Z.; Zhang, E.; Liang, B.; Chen, X.; Huang, Z. EXO1 Plays a Carcinogenic Role in Hepatocellular Carcinoma and Is Related to the Regulation of FOXP3. *J. Cancer* **2020**, *11*, 4917−4932.
(70) Liu, B.; Zhang, G.; Cui, S.; Du, G. Upregulation of KIF11 in TP53 Mutant Glioma Promotes Tumor Stemness and Drug Resistance. *Cell. Mol. Neurobiol.* **2022**, *42*, 1477−1485.
(71) Jiang, C.; Zhang, H.; Wu, W.; Wang, Z.; Dai, Z.; Zhang, L.; Liu, Z.; Cheng, Q. Immune Characteristics of LYN in Tumor Microenvironment of Gliomas. *Front. Cell Dev. Biol.* **2022**, *9*, 760929.
(72) Xue, Q.; Cao, C.; Chen, X. Y.; Zhao, J.; Gao, L.; Li, S. Z.; Fei, Z. High Expression of MMP9 in Glioma Affects Cell Proliferation and Is Associated with Patient Survival Rates. *Oncol. Lett.* **2017**, *13*, 1325.
(73) Liu, J.; Yang, X.; Ji, Q.; Yang, L.; Li, J.; Long, X.; Ye, M.; Huang, K.; Zhu, X. Immune Characteristics and Prognosis Analysis of the Proteasome 20S Subunit Beta 9 in Lower-Grade Gliomas. *Front. Oncol.* **2022**, *12*, 875131.
(74) Smith, S. J.; Li, C. M.; Lingeman, R. G.; Hickey, R. J.; Liu, Y.; Malkas, L. H.; Raoof, M. Molecular Targeting of Cancer-Associated PCNA Interactions in Pancreatic Ductal Adenocarcinoma Using a Cell-Penetrating Peptide. *Mol. Ther. Oncolytics* **2020**, *17*, 250−256.
(75) Aaberg-Jessen, C.; Fogh, L.; Sørensen, M. D.; Halle, B.; Brünner, N.; Kristensen, B. W. Overexpression of TIMP-1 and Sensitivity to Topoisomerase Inhibitors in Glioblastoma Cell Lines. *Pathol. Oncol. Res.* **2019**, *25*, 59−69.
(76) Wang, B. Q.; Zhang, C. M.; Gao, W.; Wang, X. F.; Zhang, H. L.; Yang, P. C. Cancer-Derived Matrix Metalloproteinase-9 Contributes to Tumor Tolerance. *J. Cancer Res. Clin. Oncol.* **2011**, *137*, 1525−1533.
(77) Juric, V.; O'Sullivan, C.; Stefanutti, E.; Kovalenko, M.; Greenstein, A.; Barry-Hamilton, V.; Mikaelian, I.; Degenhardt, J.; Yue, P.; Smith, V.; Mikels-Vigdal, A. MMP-9 Inhibition Promotes Anti-Tumor Immunity through Disruption of Biochemical and Physical Barriers to T-Cell Trafficking to Tumors. *PLoS One* **2018**, *13*, No. e0207255.

https://doi.org/10.1021/acsomega.3c00441
ACS Omega 2023, 8, 10565−10590

(78) van Tellingen, O.; Yetkin-Arik, B.; de Gooijer, M. C.; Wesseling, P.; Wurdinger, T.; de Vries, H. E. Overcoming the Blood-Brain Tumor Barrier for Effective Glioblastoma Treatment. *Drug Resist. Updates* **2015**, *19*, 1−12.
(79) Ursu, O.; Rayan, A.; Goldblum, A.; Oprea, T. I. Understanding Drug-Likeness. *Wiley Interdiscip. Rev. Comput. Mol. Sci.* **2011**, *1*, 760−781.
(80) Yang, Z. Y.; Yang, Z. J.; He, J. H.; Lu, A. P.; Liu, S.; Hou, T. J.; Cao, D. S. Benchmarking the Mechanisms of Frequent Hitters: Limitation of PAINS Alerts. *Drug Discov. Today* **2021**, *26*, 1353−1358.
(81) Guan, L.; Yang, H.; Cai, Y.; Sun, L.; Di, P.; Li, W.; Liu, G.; Tang, Y. ADMET-Score − a Comprehensive Scoring Function for Evaluation of Chemical Drug-Likeness. *MedChemComm* **2019**, *10*, 148.
(82) Zhu, R.; Hu, L.; Li, H.; Su, J.; Cao, Z.; Zhang, W. Novel Natural Inhibitors of CYP1A2 Identified by in Silico and in Vitro Screening. *Int. J. Mol. Sci.* **2011**, *12*, 3250.
(83) Durán-Iturbide, N. A.; Díaz-Eufracio, B. I.; Medina-Franco, J. L. In Silico ADME/Tox Profiling of Natural Products: A Focus on BIOFACQUIM. *ACS Omega* **2020**, *5*, 16076−16084.
(84) Lei, T.; Chen, F.; Liu, H.; Sun, H.; Kang, Y.; Li, D.; Li, Y.; Hou, T. ADMET Evaluation in Drug Discovery. Part 17: Development of Quantitative and Qualitative Prediction Models for Chemical-Induced Respiratory Toxicity. *Mol. Pharm.* **2017**, *14*, 2407−2421.
(85) Shen, K. H.; Hung, J. H.; Chang, C. W.; Weng, Y. T.; Wu, M. J.; Chen, P. S. Solasodine Inhibits Invasion of Human Lung Cancer Cell through Downregulation of MiR-21 and MMPs Expression. *Chem. Biol. Interact.* **2017**, *268*, 129−135.
(86) Liu, N.; Wang, X.; Wu, H.; Lv, X.; Xie, H.; Guo, Z.; Wang, J.; Dou, G.; Zhang, C.; Sun, M. Computational Study of Effective Matrix Metalloproteinase 9 (MMP9) Targeting Natural Inhibitors. *Aging* **2021**, *13*, 22867−22882.
(87) Mao, Y.; Feng, Q.; Zheng, P.; Yang, L.; Liu, T.; Xu, Y.; Zhu, D.; Chang, W.; Ji, M.; Ren, L.; Wei, Y.; He, G.; Xu, J. Low Tumor Purity Is Associated with Poor Prognosis, Heavy Mutation Burden, and Intense Immune Phenotype in Colon Cancer. *Cancer Manage. Res.* **2018**, *10*, 3569.
(88) Gong, Z.; Zhang, J.; Guo, W. Tumor Purity as a Prognosis and Immunotherapy Relevant Feature in Gastric Cancer. *Cancer Med.* **2020**, *9*, 9052−9063.
(89) Zhao, Y.; Zhang, X.; Yao, J. Comprehensive Analysis of PLOD Family Members in Low-Grade Gliomas Using Bioinformatics Methods. *PLoS One* **2021**, *16*, No. e0246097.
(90) Dai, Y.; Siemann, D. C-Src Is Required for Hypoxia-Induced Metastasis-Associated Functions in Prostate Cancer Cells. *OncoTargets Ther.* **2019**, *12*, 3519.
(91) Baek, J.-H.; Birchmeier, C.; Zenke, M.; Hieronymus, T. The HGF Receptor/Met Tyrosine Kinase Is a Key Regulator of Dendritic Cell Migration in Skin Immunity. *J. Immunol.* **2012**, *189*, 1699−1707.
(92) Yang, I.; Tihan, T.; Han, S. J.; Wrensch, M. R.; Wiencke, J.; Sughrue, M. E.; Parsa, A. T. CD8+ T-Cell Infiltrate in Newly Diagnosed Glioblastoma Is Associated with Long-Term Survival. *J. Clin. Neurosci.* **2010**, *17*, 1381.
(93) Kalaora, S.; Lee, J. S.; Barnea, E.; Levy, R.; Greenberg, P.; Alon, M.; Yagel, G.; Bar Eli, G.; Oren, R.; Peri, A.; Patkar, S.; Bitton, L.; Rosenberg, S. A.; Lotem, M.; Levin, Y.; Admon, A.; Ruppin, E.; Samuels, Y. Immunoproteasome Expression Is Associated with Better Prognosis and Response to Checkpoint Therapies in Melanoma. *Nat. Commun.* **2020**, *11*, 896.
(94) Han, J.; Jing, Y.; Han, F.; Sun, P. Comprehensive Analysis of Expression, Prognosis and Immune Infiltration for TIMPs in Glioblastoma. *BMC Neurol.* **2021**, *21*, 447.
(95) Xu, B. Prediction and Analysis of Hub Genes between Glioblastoma and Low-Grade Glioma Using Bioinformatics Analysis. *Medicine* **2021**, *100*, No. e23513.
(96) Tornillo, G.; Knowlson, C.; Kendrick, H.; Cooke, J.; Mirza, H.; Aurrekoetxea-Rodríguez, I.; Vivanco, M. d. M.; Buckley, N. E.; Grigoriadis, A.; Smalley, M. J. Dual Mechanisms of LYN Kinase Dysregulation Drive Aggressive Behavior in Breast Cancer Cells. *Cell Rep.* **2018**, *25*, 3674−3692.
(97) Liu, H.; Chen, D.; Liu, P.; Xu, S.; Lin, X.; Zeng, R. Secondary Analysis of Existing Microarray Data Reveals Potential Gene Drivers of Cutaneous Squamous Cell Carcinoma. *J. Cell. Physiol.* **2019**, *234*, 15270−15278.
(98) Edwards, L. A.; Woo, J.; Huxham, L. A.; Verreault, M.; Dragowska, W. H.; Chiu, G.; Rajput, A.; Kyle, A. H.; Kalra, J.; Yapp, D.; Yan, H.; Minchinton, A. I.; Huntsman, D.; Daynard, T.; Waterhouse, D. N.; Thiessen, B.; Dedhar, S.; Bally, M. B. Suppression of VEGF Secretion and Changes in Glioblastoma Multiforme Microenvironment by Inhibition of Integrin-Linked Kinase (ILK). *Mol. Cancer Ther.* **2008**, *7*, 59−70.
(99) Gazon, H.; Barbeau, B.; Mesnard, J. M.; Peloponese, J. M. Hijacking of the AP-1 Signaling Pathway during Development of ATL. *Front. Microbiol.* **2018**, *8*, 2686.
(100) Okura, H.; Golbourn, B. J.; Shahzad, U.; Agnihotri, S.; Sabha, N.; Krieger, J. R.; Figueiredo, C. A.; Chalil, A.; Landon-Brace, N.; Riemenschneider, A.; Arai, H.; Smith, C. A.; Xu, S.; Kaluz, S.; Marcus, A. I.; Van Meir, E. G.; Rutka, J. T. A Role for Activated Cdc42 in Glioblastoma Multiforme Invasion. *Oncotarget* **2016**, *7*, 56958.
(101) Zagzag, D.; Lukyanov, Y.; Lan, L.; Ali, M. A.; Esencay, M.; Mendez, O.; Yee, H.; Voura, E. B.; Newcomb, E. W. Hypoxia-Inducible Factor 1 and VEGF Upregulate CXCR4 in Glioblastoma: Implications for Angiogenesis and Glioma Cell Invasion. *Lab. Invest.* **2006**, *86*, 1221−1232.
(102) Amaral, R. F.; Geraldo, L. H. M.; Einicker-Lamas, M.; e Spohr, T. C. L. d. S.; Mendes, F.; Lima, F. R. S. Microglial Lysophosphatidic Acid Promotes Glioblastoma Proliferation and Migration via LPA1 Receptor. *J. Neurochem.* **2021**, *156*, 499−512.
(103) Harper, K.; Lavoie, R. R.; Charbonneau, M.; Brochu-Gaudreau, K.; Dubois, C. M. The Hypoxic Tumor Microenvironment Promotes Invadopodia Formation and Metastasis through LPA1 Receptor and EGFR Cooperation. *Mol. Cancer Res.* **2018**, *16*, 1601−1613.
(104) Quintero-Fabián, S.; Arreola, R.; Becerril-Villanueva, E.; Torres-Romero, J. C.; Arana-Argáez, V.; Lara-Riegos, J.; Ramírez-Camacho, M. A.; Alvarez-Sánchez, M. E. Role of Matrix Metalloproteinases in Angiogenesis and Cancer. *Front. Oncol.* **2019**, *9*, 1370.
(105) Kessenbrock, K.; Plaks, V.; Werb, Z. Matrix Metalloproteinases: Regulators of the Tumor Microenvironment. *Cell* **2010**, *141*, 52.
(106) Petrova, V.; Annicchiarico-Petruzzelli, M.; Melino, G.; Amelio, I. The Hypoxic Tumour Microenvironment. *Oncogenesis* **2018**, *7*, 10.
(107) Jana, S.; Singh, S. K. Identification of Selective MMP-9 Inhibitors through Multiple e-Pharmacophore, Ligand-Based Pharmacophore, Molecular Docking, and Density Functional Theory Approaches. *J. Biomol. Struct. Dyn.* **2019**, *37*, 944−965.
(108) Yamamoto, D.; Takai, S.; Jin, D.; Inagaki, S.; Tanaka, K.; Miyazaki, M. Molecular Mechanism of Imidapril for Cardiovascular Protection via Inhibition of MMP-9. *J. Mol. Cell. Cardiol.* **2007**, *43*, 670−676.
(109) Yamamoto, D.; Takai, S.; Hirahara, I.; Kusano, E. Captopril Directly Inhibits Matrix Metalloproteinase-2 Activity in Continuous Ambulatory Peritoneal Dialysis Therapy. *Clin. Chim. Acta* **2010**, *411*, 762−764.
(110) Kast, R. E.; Halatsch, M. E. Matrix Metalloproteinase-2 and -9 in Glioblastoma: A Trio of Old Drugs—Captopril, Disulfiram and Nelfinavir—Are Inhibitors with Potential as Adjunctive Treatments in Glioblastoma. *Arch. Med. Res.* **2012**, *43*, 243−247.
(111) Lastakchi, S.; Olaloko, M. K.; McConville, C. A Potential New Treatment for High-Grade Glioma: A Study Assessing Repurposed Drug Combinations against Patient-Derived High-Grade Glioma Cells. *Cancers* **2022**, *14*, 2602.
(112) Jiang, Q. W.; Chen, M. W.; Cheng, K. J.; Yu, P. Z.; Wei, X.; Shi, Z. Therapeutic Potential of Steroidal Alkaloids in Cancer and Other Diseases. *Med. Res. Rev.* **2016**, *36*, 119−143.
(113) Jiang, G.; Zhang, L.; Wang, J.; Zhou, H. Baicalein Induces the Apoptosis of U251 Glioblastoma Cell Lines via the NF-KB-P65-Mediated Mechanism Baicalein Induces the Apoptosis of U251 Glioblastoma Cell Lines via the NF-KB-P65-Mediated Mechanism. *Anim. Cell Syst.* **2016**, *20*, 296.

https://doi.org/10.1021/acsomega.3c00441
ACS Omega 2023, 8, 10565−10590

(114) Zhai, K.; Mazurakova, A.; Koklesova, L.; Kubatka, P.; Büsselberg, D. Flavonoids Synergistically Enhance the Anti-Glioblastoma Effects of Chemotherapeutic Drugs. *Biomolecules* **2021**, *11*, 1841.
(115) Xue, W.; Wang, P.; Tu, G.; Yang, F.; Zheng, G.; Li, X.; Li, X.; Chen, Y.; Yao, X.; Zhu, F. Computational Identification of the Binding Mechanism of a Triple Reuptake Inhibitor Amitifadine for the Treatment of Major Depressive Disorder. *Phys. Chem. Chem. Phys.* **2018**, *20*, 6606−6616.
(116) Khanal, P.; Dey, Y. N.; Patil, R.; Chikhale, R.; Wanjari, M. M.; Gurav, S. S.; Patil, B. M.; Srivastava, B.; Gaidhani, S. N. Combination of System Biology to Probe the Anti-Viral Activity of Andrographolide and Its Derivative against COVID-19. *RSC Adv.* **2021**, *11*, 5065−5079.
(117) Awale, S.; Miyamoto, T.; Linn, T. Z.; Li, F.; Win, N. N.; Tezuka, Y.; Esumi, H.; Kadota, S. Cytotoxic Constituents of Soymida Febrifuga from Myanmar. *J. Nat. Prod.* **2009**, *72*, 1631−1636.
(118) Sowmyya, T.; Vijaya Lakshmi, G. Antimicrobial and Catalytic Potential of Soymida Febrifuga Aqueous Fruit Extract-Engineered Silver Nanoparticles. *Bionanoscience* **2018**, *8*, 179−195.
(119) Lim, M.; Xia, Y.; Bettegowda, C.; Weller, M. Current State of Immunotherapy for Glioblastoma. *Nat. Rev. Clin. Oncol.* **2018**, *15*, 422−442.
(120) Lee, Y.-L.; Cheng, W.-E.; Chen, S.-C.; Chen, C.; Shih, C.-M. The Effects of Hypoxia on the Expression of MMP-2, MMP-9 in Human Lung Adenocarcinoma A549 Cells. *Eur. Respir. J.* **2014**, *44*, P2699.
(121) Bauer, A. T.; Bürgers, H. F.; Rabie, T.; Marti, H. H. Matrix Metalloproteinase-9 Mediates Hypoxia-Induced Vascular Leakage in the Brain via Tight Junction Rearrangement. *J. Cerebr. Blood Flow Metabol.* **2010**, *30*, 837.

https://doi.org/10.1021/acsomega.3c00441
ACS Omega 2023, 8, 10565−10590